

Contents

	Acknowledgements	i
	Résumé	iii
	Abstract	v
	Contents	ix
1	Introduction	1
1.1	From a single galaxy to an expanding Universe	1
1.2	The large scale structure of the Universe	4
1.3	From the cosmic web to galaxy formation	5
2	Context	9
2.1	Cosmology	9
2.1.1	Properties of the initial conditions of the Universe	9
2.1.2	Formation of the structures of the Universe	15
2.1.3	The excursion set theory	21
2.1.4	The upcrossing approximation to $f(\sigma)$	23
2.1.5	The peak patch theory	25
2.1.6	Tidal torque theory	28
2.1.7	Description of the field	29
2.2	Galaxy formation	31
2.2.1	Classical model of galaxy formation	32
2.2.2	Baryonic processes	33
2.2.3	Numerical simulations	39
2.3	Synopsis	49



1. Introduction

1.1 From a single galaxy to an expanding Universe

From the 18th century, most of the observed objects in the sky were thought to be located in a single entity – the Milky Way – whose borders were the borders of the Universe. Setting apart planets and stars, these objects were broadly classified as *nebulæ*, from the latin word for cloud or fog, as they resemble diffuse clouds in sky. In 1771, Charles Messier published his “Catalogue des Nébuleuses et des Amas d’Étoiles” (Catalogue of Nebulæ and Star Clusters). Charles Messier first interest was in comets, but in order to observe them, he had to be able to distinguish moving objects from fixed objects in the sky, such as stars, star clusters and *nebulæ*. This led him to systematically compile a list of the objects in the sky that were impairing his observations. This catalogue, known as the Messier Catalogue is still today one of the most popular catalogues among amateur astronomers.

With the advent of better observations and the systematic classification of the objects, astronomers started distinguishing star clusters from diffuse *nebulæ* from spiral *nebulæ*. During the 18th and 19th centuries, many philosophers and mathematicians (E. Swedenborg, P.L. Maupertuis, T. Wright) speculated that the Milky Way is itself a “spiral nebula”, made of a flattened disk of stars and that the spiral *nebulæ* are its analogues, but reside outside the Milky Way, while others argued that the spiral *nebulæ* were part of the Milky Way. This questioned not only the location of the Milky way and the spiral *nebulæ* in space, but also their relative sizes. However, observational evidences were missing to rule out any of the two models and it was not until the 20th century that it was finally shown that these *nebulæ* live outside of the Milky Way. One of the first proofs of the extra-galactic nature of the *nebulæ* can be attributed to Vesto Slipher. In 1912, he made spectrographic observations of the brightest spiral *nebulæ* ; all of them showed significant Doppler shifts, suggesting that the *nebulæ* are receding at velocities of hundreds to thousands of kilometres per seconds, much greater than the relative velocities of the stars of the Milky way. In 1917, observations of supernovæ in the Great Andromeda Nebula (now called the Andromeda galaxy) revealed that the supernovæ were 10 magnitudes fainter than supernovæ in the Milky Way, suggesting that they were much further away than the ones observed in the Milky Way. Using conservative assumptions, Shapley and Curtis, 1921 estimated that the Andromeda

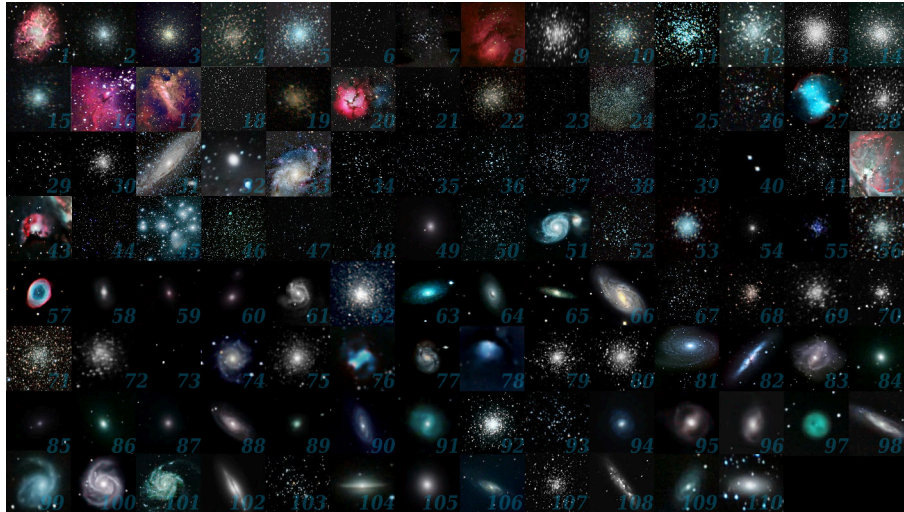


Figure 1.1.1: The 110 objects of the Messier catalogue, taken and compiled by an amateur astronomer. Credits: Michael A. Phillips.

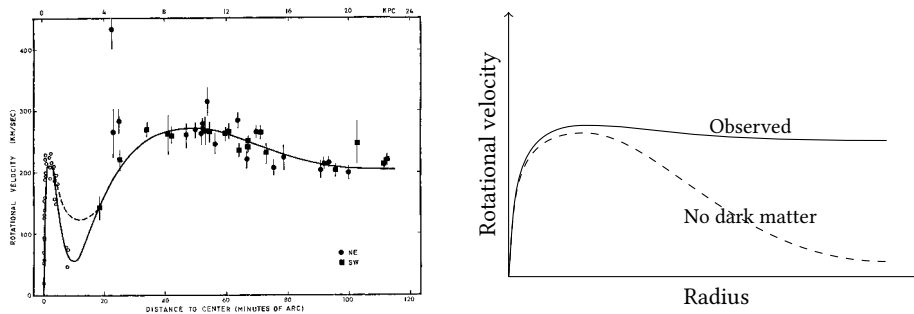


Figure 1.1.2: *Left:* Rotational profile of the Andromeda galaxy from Rubin and Ford, 1970. *Right:* Scheme of the rotational velocity profile. The expected rotational velocity profile with no dark matter is shown as a dashed line, the observed rotational profile is shown as a solid line. Without dark matter, the rotation profile decreases after some radius while the addition of dark matter makes the profile flatter at large radii, in agreement with observations.

Nebula could not be any closer than 20 000 ly, but still 7 000 ly off the plane of the Milky way. This was further confirmed by the distance estimations of the nebulae by Edwin Hubble, which definitely showed that nebulae were too distant to be part of the Milky Way. We now call spiral (and elliptical) nebulae “galaxies” from the greek words γάλα (“milk”) and ζίας (“way”).

In 1929, Hubble was able to show that galaxies were receding at increasing velocities with increasing distance, so that galaxies further away are receding faster, a relation now known as Hubble-Lemaître’s law. The law states that the receding velocity is proportional to the distance times the Hubble constant H . Even though the measurements were largely inaccurate – Hubble’s measurements gave $H = 500 \text{ km/s/Mpc}$ while modern estimates are around 70 km/s/Mpc – the result showed that the Universe is not only made of multiple galaxies, but it is also expanding, paving the way to modern cosmology. At this point, the basic building blocks of the Universe were broadly found: the Universe is made of a multitude of individual galaxies, each of which has millions to several hundred billions stars, and sizes of the order of 10 kly to 100 kly, while the distances between galaxies are of the order of the Mly.

The next step in our current understanding of the structure of galaxies and cosmology appeared

in the course of the 20th century. The discoveries of the distances and sizes of galaxies was shortly followed by estimations of their mass. In order to do so, a simple way is to use the laws of gravity: objects orbiting massive objects have smaller periods according to Kepler's laws. By measuring the velocities of objects gravitating in or around galaxies, one can infer their *gravitational* mass. Since galaxies are made of stars, one can also estimate the stellar mass from the galaxies' apparent luminosity. The ratio of gravitational mass required to explain the observed velocities to the observed stellar mass, known as the "mass-to-light" ratio was initially thought to be one. However, observations in the 1920s showed that the mass required to explain the motion of stars in the neighbourhood of the Sun is much larger than the observed one. Later in the 1930s, observations of the motion of galaxies in the Coma cluster led to the same conclusion that the gravitational mass should be much larger than the observed ones. These evidences were later confirmed when Rubin and Ford, 1970 showed that most of the mass of galaxies is not in stars. This was shown by measuring the rotational velocity of stars in the Andromeda galaxy. If the bulk of the mass of the galaxy was due to its stars, then the rotational velocity should increase from the centre to a radius of 10 000 ly, reaching a maximum of ~ 200 km/s before decreasing. The observations however showed that the rotation curve rises as a function of radius before reaching a plateau at a radius of 10 000 ly at about 250 km/s, as shown on figure 1.1.2, left panel. This discovery, followed by multiple similar results, all confirmed that most of the mass in galaxies – and similarly in galaxy cluster – is hidden and is invisible. This matter that interacts *via* gravity but cannot be seen is now called Dark Matter (DM). In order to match observations, galaxies should be embedded in an extended DM halo, so that the decrease of stellar density with increasing radius is mitigated by the extended dark matter halo in the outskirts of the galaxy. This is schematically illustrated on figure 1.1.2, right panel. In addition to a correct distance ladder, astronomers now had access to a mass scale, albeit imprecise: in addition to the billion of stars that make galaxies, an extended and massive halo of dark matter surrounds each galaxy.

At about the same time other evidences for dark matter emerged with the discovery of the Cosmic Microwave Background (CMB) by Penzias and Wilson, 1965. This electromagnetic emission, emitted at the infancy of the Universe, shows that the Universe started in a quasi-homogeneous hot and dense state, with tiny density fluctuations of the order of the 10^{-4} to 10^{-5} . In a model missing dark matter, these initial density fluctuations would be too small for gravitational collapse to have time to pull matter together and form the observed large structure of the Universe. This is a consequence of the interaction of baryonic matter with radiation: up to the emission of the CMB, gravitational collapse was prevented due to the radiative pressure of photons scattering from atoms to atoms. Dark matter provides a solution to the problem because it does not interact with light. Therefore, its density perturbations can grow first and create a potential well into which baryonic structures will later collapse. In addition to the CMB observations, several other observations such as gravitational lensing by galaxy clusters or the temperature distribution of hot gas in galaxies and clusters all pointed towards dark matter.

These discoveries, in conjunction with the development of general relativity led to the emergence of the standard model of cosmology, the Λ Cold Dark Matter (Λ CDM) model. The Λ CDM describes the evolution of the Universe after the CMB and is made of the following building bricks

1. the CMB is described by a Gaussian random field with known statistical properties,
2. the Universe is homogeneous and isotropic with no spatial curvature,
3. the Universe contains dark energy (Λ term), cold dark matter (CDM) in addition to ordinary matter and radiation.

According to the Λ CDM, the Universe started from a hot dense state some 14 Gyr ago and has been expanding since then, as measured by Hubble, 1929 and is now in accelerated expansion, as a result of non-null Λ term in Einstein's equations. About 85 % of the current matter of the Universe is DM, the remaining 15 % being ordinary baryonic matter (gas, stars, etc.). All this matter only

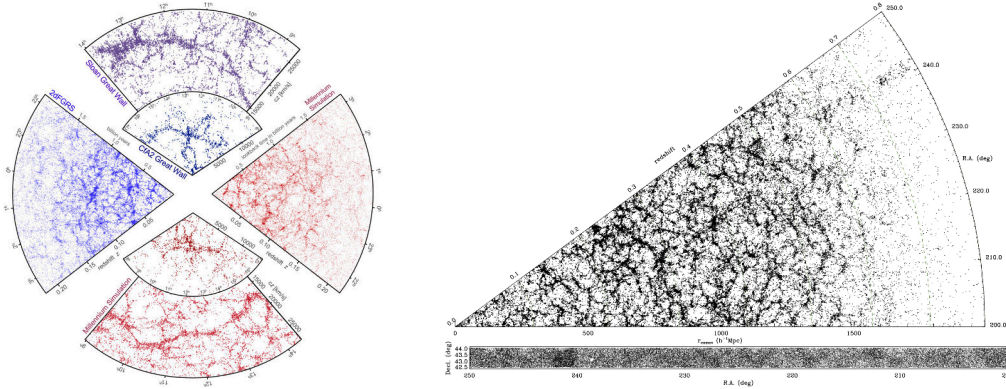


Figure 1.2.1: (Left:) The galaxy distribution obtained from spectroscopic redshift surveys (blue) and from mock catalogues (red) constructed from cosmological simulations. From Springel et al., 2006. (Right:) Catalogue of the spectroscopic HectoMAP survey in the local Universe (Hwang et al., 2016). The cosmic web made of large voids, filaments and dense nodes is clearly visible.

adds up to 30 % of the total energy density of the current Universe, the remaining 70 % being dark energy. The success of the Λ CDM is well illustrated by the advent of the “precision cosmology” era, in which the parameters of the model can be fitted to observations down to percent levels using a variety of measurements, from CMB observations (Bennett et al., 2013; Planck Collaboration, 2018a), baryonic acoustic oscillations (e.g. Eisenstein et al., 2005; Moresco et al., 2016; Alam et al., 2017), type Ia supernovae (e.g. Riess et al., 1998; Perlmutter et al., 1999; Abbott et al., 2019), weak lensing, cluster abundances (see e.g. Weinberg et al., 2013, and references therein for a detailed review).

1.2 The large scale structure of the Universe

Since the assumption of homogeneity clearly breaks down on small scales, as revealed by the presence of galaxies or stars, there must be certain homogeneities present at a certain time in history of the Universe. The homogeneities can be traced back in time to the CMB, but also to much larger scales, as can be seen in galaxy surveys that have revealed the existence of superstructures (cluster of galaxies, super-clusters and filaments and walls connecting them) on scales up to a few tens to hundreds of Mpc¹, as can be seen on figure 1.2.1. While each of these structures, from galaxies to super clusters or filaments, is unique in its morphology and mass, their overall statistical properties are homogeneous: the probability of any configuration is independent on the spatial location. Recent surveys, like the Sloan Digital Sky Survey (Abazajian et al., 2003), the 2MASS redshift survey (Huchra et al., 2012) or HectoMap (Hwang et al., 2016) have improved significantly our knowledge of the galaxy distribution showing with no doubt that galaxies form a complex web-like network on large scales made of voids, walls and filaments that interconnect with clusters of galaxies. This pattern is known as the *cosmic web*.

Due to the laws of gravity, the initial tiny fluctuations evolved into large and complex anisotropic structures that shape the current Universe. At scales of up to a few tens of Mpc, large under-dense regions called voids are found (Pan et al., 2012). Put together, the voids form a foam-like structure where each bubble is bound by denser walls or pancakes, sometimes called Zel’dovich pancakes (Zeldovich, 1970). The initial motion of particles can be well approximated in their linear regime by a rectilinear trajectory where the direction is set by the initial tides.

¹The pc length unit is commonly used in astronomy, where $1 \text{ pc} \approx 3.08 \times 10^{16} \text{ m} \approx 3.3 \text{ ly}$

Similar to parallel light rays bent by a disturbed water surface, the particles will travel until they form caustics. The first caustics to form, resulting from the collapse of matter along one direction, are bi-dimensional in nature. Following this first collapse, a second direction may collapse to form secondary caustics, resulting in uni-dimensional filamentary structures. Finally, filamentary structures may also collapse to form “knots” or nodes of the cosmic web.

As the cosmic web builds up, dense and spheroidal regions will undergo spherical collapse, resulting in the formation of dark matter halos. These primordial halos will later merge to form larger halos that in turn will also merge. This continuous accretion and successive merger scenario is often referred to as hierarchical formation. In classical models, galaxies form in (sub-)halos (Kauffmann et al., 1993) themselves located in the cosmic web. The distribution of galaxies in the Universe follows that of the large-scale structures as most of them are found in walls, filaments and nodes of the cosmic web. Recent developments have also shown that not only does the spatial distribution of galaxies relate to the cosmic web, but also some of their properties such as the orientation of their spin or their colour.

1.3 From the cosmic web to galaxy formation

According to the classical galaxy formation paradigm, gas falling on a proto-galaxy heats up to the Virial temperature of its host halo when crossing the virial radius (Rees and Ostriker, 1977; Silk, 1977). In this scenario, the gas acquires the same angular momentum distribution as dark matter before turning around and flowing towards the proto-galaxy, which has been confirmed by hydrodynamic simulations that do not describe cooling (e.g. van den Bosch et al., 2002). This process of angular momentum acquisition, at the core of the understanding of the formation of disk galaxies at high redshift, is well explained by the Tidal Torque Theory (TTT, Peebles, 1969; Doroshkevich, 1973; S. D. M. White, 1984). It predicts that the angular momentum of the dark matter increases under the effect of the gravitational torques of the cosmic web before dark matter decouples from the expansion of the Universe. In the classic scenario, the gas undergoes the same tidal field before decoupling but loses all dynamical and causal connection with the large scale structures at the Virial radius. Following this idea, classical models of galaxy formation typically ignore any coupling of the baryons to their large scale environment, so that galaxy properties are directly inherited from the mass history of their host halo or some quantities averaged over all angles. While such scenario has proven quite successful in explaining many observed properties of galaxies, via the so-called halo model (see Cooray and R. Sheth, 2002, for a detailed review), in particular against isotropic statistics such as the two-point correlation function, it fails to capture some galactic properties, such as spin alignments, which are specifically driven by scale-coupling to the cosmic web (Codis et al., 2015), nor does it fully take into account how a given galaxy is gravitationally sensitive to the larger scales anisotropies. Indeed, when gas cooling is accounted for, it has been shown that a substantial part of the baryon mass and angular momentum is acquired via cold filamentary flows (Birnboim and Dekel, 2003; Ocvirk et al., 2008; Dekel et al., 2009; Kereš et al., 2009), feeding the galaxy in a highly anisotropic way. Unlike shock-heated gas, cold flows are able to penetrate halos to reach their innermost regions, feeding galaxies with pristine fuel for star formation. A three-dimensional visualization of galactic formation processes at intermediate scales (made possible by the joint use of tracer particles for the cold gas phase, and well-resolved zoom simulations) reveals that these gaseous flows stem from the cosmic web. In fact, the spatial distribution of caustics (the geometric location of the dark matter shell crossing and the isothermal shock of cold gas) provides us with direct information on the dynamical state of the gas likely to be accreted on the proto-galaxy: in this scenario, the gas first flows towards the caustics created by the dark matter to form wall-like structures, in which galaxies are embedded (Danovich et al., 2012). The gas then radiatively cools and loses its velocity component in the direction perpendicular to the walls to condense at the center of dark matter filaments found

at the intersection of walls. In the process, the gas retains a net transverse motion that sets the direction and amplitude of its angular momentum which will later be fed coherently into growing proto-galaxies. Doing so, it retains its angular momentum – and hence its causal connection to the cosmic web – until it reaches the innermost part of the galaxy (Pichon et al., 2011; Danovich et al., 2015), providing a unique testbed to assess the effect of the cosmic web on the formation of galaxies.

With the advent of large spectroscopic surveys (GAMA, Driver et al., 2011; VIPERS, Guzzo et al., 2014) and cosmological simulations (Illustris, Vogelsberger et al., 2014; Eagle, Schaye et al., 2015; Massive-Black II, Khandai et al., 2015; Horizon-AGN Dubois et al., 2014; Dubois et al., 2016), astronomers can now explore time modulations of the galactic properties with statistically meaningful data, but also their spatial modulations in the frame of the cosmic web (e.g. Alpaslan et al., 2016; Malavasi et al., 2017; Laigle et al., 2018; Kraljic et al., 2019). There is now a dire need for both new methods and models to understand the coupling between the anisotropic cosmic web and the baryonic physics of galaxies. In particular one needs to build new estimators to quantify the spatial modulation of galaxy properties beyond isotropic two-point correlation functions on top of the classical halo model. As the effect of the cosmic web is expected to be a second-order (after mass and local density dependence), new estimators and models have to be built that take into account explicitly the anisotropy of the cosmic web to prevent the signal from being lost when averaging over all possible angles.

The aim of this dissertation is to provide such estimators and models, with a novel framework devoted to the study of the effect of anisotropic features on the formation of dark matter halos and their galaxies. The approach followed in my work is two-fold: I study the effect of the cosmic web on large and small scales on the assembly of dark matter halos across cosmic time using conditional excursion set and critical set theory and use numerical simulations to unveil how these effects impact galaxy formation.

Chapter 2 describes the context on which this dissertation is based, presenting the different models and tools used in the course of my work. Chapter 3 presents an extension of the excursion set theory and predicts the accretion rate, formation times and typical masses of dark matter halos as a function of their environment. Chapter 4 presents a framework based on the peak theory to quantify the environmental effects acting on halo formation. In particular, it aims to provide a comprehensive of the major events relevant to the assembly of galaxies. Chapter 5 presents a new numerical scheme able to accurately track the cosmic accretion in cosmological simulation. Chapter 6 presents results obtained from a numerical study of how angular momentum is acquired from the cosmic web and transported towards galaxies *via* cold flows. Chapter 7 wraps things up and discusses perspectives.

Disclaimer

The results presented in chapter 3 have led to a publication in MNRAS (Musso, Cadiou et al., 2018). I have produced all the results of the paper in collaboration with M. Musso, with contributions from C. Pichon, S. Codis, K. Kraljic and Y. Dubois.

The results presented in chapter 4 have been obtained in collaboration with C. Pichon and S. Codis, with contributions from D. Pogosyan, Y. Dubois and M. Musso.

The results presented in chapter 5 have led to a publication in A&A (Cadiou et al., 2019). I have produced all the results of the paper, with contributions from Y. Dubois and C. Pichon.

I have produced all the results of chapter 6, with contributions from Y. Dubois and C. Pichon.

I have read and contributed to all publications presented in appendix B, albeit not as the main author. More specifically, I contributed to the theoretical sections of Kraljic et al., 2018; Kraljic et al., 2019. I contributed to the numerical setup of Beckmann et al., submitted by providing the tracer particle code.

To the best of my knowledge, all the results presented in the dissertation are original.

2.3 Synopsis

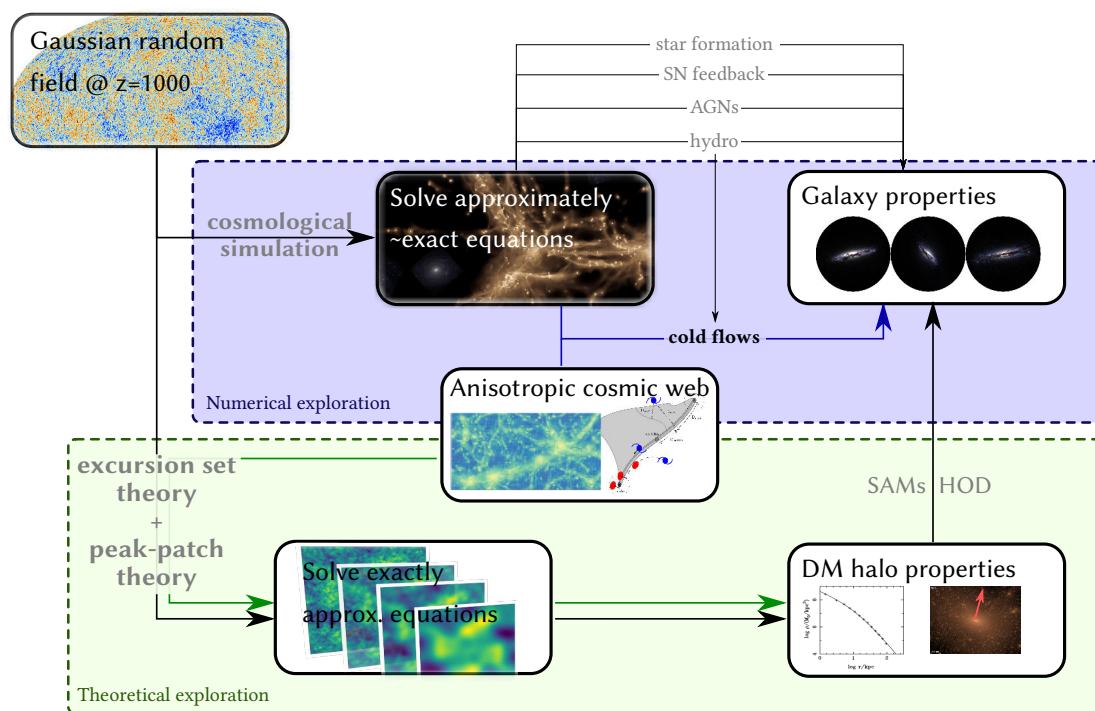


Figure 2.3.1: Scheme of the approaches used in this thesis to study the formation of dark matter halos and galaxies. The different processes relevant to the formation of dark matter halos and their galaxies are shown in gray. The two axes developed in the thesis are shown in the green area (theoretical exploration, chapter 4) and blue area (numerical exploration, chapter 6). In the former, I developed extensions to the excursion set and peak theory that explicitly include the anisotropic effect of the cosmic web. This was used to predict environmental-driven effects on the properties of DM halos. In the latter, I developed numerical methods to accurately follow the cosmic accretion of gas in simulations and applied it to understand how angular momentum is transported by cold flows on high-redshift galaxies.

In Section 2.1, I have presented the cosmological context in which galaxies form. In section 2.1.1, I have presented the current evidences that the Universe is organised at large-scales in the so-called “cosmic-web”. The remaining of the dissertation will in particular focus on the link between the cosmic web and the formation of dark halos and their galaxies. In order to do so, I have presented the different tools I have used in my work. From a theoretical perspective, one can predict properties of dark matter halos from first principle using the excursion set theory, as presented in sections 2.1.3 and 2.1.4 and the peak-patch theory, as presented section 2.1.5. These tools enable us to compute the properties of dark matter halos, yet they fail at predicting the fate of baryons in galaxies. One way to study the evolution of baryons is to rely on hydrodynamical numerical simulations, which I presented in section 2.2. The different models used in the cosmological simulations I have used in my dissertation are detailed in section 2.2.2, while a more technical description focused on the numerical methods is provided in section 2.2.3.

In this dissertation, I focus on the interplay between the cosmic web and the formation of galaxies and their host halo, as illustrated in figure 2.3.1. I first provide an extension of the excursion set formalism that explicitly takes into account the cosmic web in chapter 3. This is

then used to quantify the effect of large-scale filamentary structure on the formation of dark matter halos. The predictions are then compared to recent results obtained from observations and numerical simulations. I then detail how peak theory can be extended to describe the evolution of the geometry of Lagrangian patch in chapter 4. The formalism is then applied to the study the number of filament feeding galaxies, and the impact of their location in the cosmic web.

I first describe a numerical method I implemented to accurately track the Lagrangian evolution of the gas in the Eulerian code RAMSES in chapter 5. The method relies on Monte-Carlo sampling to accurately reproduce mass fluxes between gas cells using tracer particles that then provide the Lagrangian history of the gas. The chapter also presents numerical methods relevant to the analysis of numerical simulations in the context of anisotropic accretion. The tools are then used in chapter 6 to explore the link between dark halos, the cosmic web and galaxy formation using numerical simulations, with a particular focus on the study of anisotropic accretion of gas on galaxies at $z \geq 2$ *via* cold flows.

3. The impact of the large scale cosmic web on assembly bias

Yohan Dubois – New Horizon collaboration

Outline

3.1	Introduction	51
3.2	“How does the cosmic web impact assembly bias?”	52
3.3	Conclusion	83

3.1 Introduction

Galaxies form and evolve within a complex network, the so-called cosmic web (Bond et al., 1996, see section 2.1.2), made of filaments embedded in sheet-like walls, surrounded by large voids and intersecting at clusters of galaxies (Jõeveer et al., 1978). Halo masses are highly dependent on their large-scale surrounding, as elegantly explained by the theory of biased clustering (Kaiser, 1984a; Efstathiou et al., 1988), such that high mass objects are preferentially found in over-dense regions near nodes (Bond and Myers, 1996; Pogosyan et al., 1996). The importance of interactions with the larger scale environment in driving their evolution has indeed recently emerged as a central tenet of halo formation theory.

It has been established that the clustering of dark matter halos, as measured by halo bias, not only depends on halo mass but also on other halo properties such as formation time, concentration, spin and ellipticity (Gao et al., 2005; Wechsler et al., 2006; Gao and S. D. M. White, 2007; Hahn et al., 2007). This effect, commonly referred to as “assembly bias” can be rephrased as follow: the clustering of dark matter halos and their properties are correlated, beyond a mere mass and density relation. Using a different approach, a growing number of evidence (Welker et al., 2014b; Kraljic et al., 2018; Kraljic et al., 2019) have since showed that some halo and galaxy properties present distinct features at different locations in the cosmic web. One striking example is spin-alignments

which have been measured for DM halos (e.g. Codis et al., 2012) and galaxies (e.g. Chisari et al., 2017), but also colour segregation of galaxies (Laigle et al., 2018; Kraljic et al., 2018; Kraljic et al., 2019).

As a filament is formally the field line that joins two maxima of the density field through a filament-type saddle point (Pogosyan et al., 2009a), studying the expected properties of galaxies and halos in the vicinity of filament-type saddle points is a sensible choice. Indeed TTT (Peebles, 1969; Schäfer, 2009) was recently revisited (Codis et al., 2015, see section 2.1.6) in the context of such anisotropic environments, biased by the presence of a filament within a wall, which is most efficiently represented by this point process of filament-type saddles. It predicts the alignment of the angular momentum distribution of the forming galaxies with the filament’s direction, and perpendicular orientation for massive population. Since spin plays an important role in the physical and morphological properties of galaxies, a signature is also expected in the properties of galaxies as a function of the longitudinal and transverse distance to this saddle.

Most of the previous theoretical work on the impact of the anisotropy of the environment on galactic assembly history, focused on dark matter halos. At a given mass, halos that are sufficiently far away from the potential wells grow by accreting their surrounding matter, leading to a correlation between the instantaneous accretion rate and the density of their environment (e.g. Zentner, 2007). On the other hand, halos close to the potential wells are expected to stall and stop to grow earlier, as their mass inflow is dynamically quenched by anisotropic tides generated in their vicinity (e.g. Dalal et al., 2008; Hahn et al., 2009; Ludlow et al., 2014; Borzyszkowski et al., 2017). Individual properties of dark matter halos, such as their mass, formation time or accretion, are thus expected to be affected by the exact position of halos within the large-scale anisotropic cosmic web.

These works underlined the role of the shear strength (a scalar quantity constructed out of the traceless shear tensor which does not correlate with the local density), measured on the same scale as the halo (Castorina et al., 2016; Paranjape et al., 2018). As tidal forces act against gravitational collapse, the shear strength encodes the delay induced by the dynamical quenching due to the environment. This has been justified as a phenomenological explanation of the scale-dependent scatter in the initial overdensity of proto-halos measured in simulations (Ludlow et al., 2014; R. K. Sheth et al., 2013) or as a theoretical consequence of the coupling between the shear and the inertia tensor which tends to slow down collapse (Bond and Myers, 1996; R. K. Sheth et al., 2001a; Del Popolo et al., 2001).

The purpose of this paper is to address the question of the environmental quenching of halos. In particular, is the cosmic web responsible for the environmental quenching of halos? What effect does it have on different variables entering the assembly of dark matter halos? In collaboration with M. Musso, we extended the excursion set theory to account for the large-scale modulations induced by a filament-type saddle point. From this, we computed the mass function and the accretion rate and formation times at fixed finale mass.

The results presented here were published in Musso, Cadiou et al., 2018.

3.2 “How does the cosmic web impact assembly bias?”

3.3 Conclusion

Let me complement the conclusions of this article in the context of this dissertation and of subsequent works.

We have shown that the excursion set theory can be extended to take into account anisotropic effects induced by the cosmic web. This can be done by constraining the statistics entering the excursion to the presence of a proto-filament at a given location, which in turn spatially modulates the mean and the variance of the field, resulting in a biasing of the excursion. From this, one can show that different quantities derived from the properties of the excursion under the anisotropic constrain, such as the halo mass function and the accretion rate and formation time at fixed final mass, become distinct function of the local mean and variance of the field, so that their modulation by the cosmic web is different.

The differential effect induced by the cosmic web can be illustrated by computing the isocontours of the different assembly variables, which can be shown to explicitly cross, as illustrated on figure 3.3.1. The figure shows that, for example, isodensity contours cross isocontours of accretion rate at fixed final mass. As a consequence, while most of the spatial variation of the accretion rate can be attributed to the modulation due to the local density surrounding a given halo, part of the variation is due to the tidal effect of the large-scale filamentary structure. The same conclusion can be drawn for the formation time and lead to the conclusion that the structure of the cosmic web, as encoded by the filament-type saddle point, drives part of the assembly bias signal. More massive halos are found in the filament compared to the surrounding void and wall, while the most massive halos are found in nodes of the cosmic web. At fixed final mass, halos forming close to the saddle are stalled and formed early, whereas those forming close to the nodes formed later and accrete more. The same hierarchy is found between wall and filaments. Similar trends have been measured for galaxies in the GAMA spectroscopic survey (Driver et al., 2011) and the HORIZON-AGN simulation in a paper I contributed to (Kraljic et al., 2018, see appendix B.1). Namely, it was shown that galaxies in filaments are more massive than their wall counterparts. In addition, galaxies also segregate by colour, with an excess of red passive galaxies close to the filament core than in the wall.

In a follow-up work (Kraljic et al., 2019, see appendix B.2), we measured the properties of virtual galaxies in the HORIZON-AGN simulation in the frame of the cosmic web, reproducing the same maps as Musso, Cadiou et al., 2018, figure 8. In this work, I have shown that the results from the constrained excursion set theory can be qualitatively reproduced if one takes into account the mean Zel'dovich displacement (following the idea of the Bond and Myers, 1996), which has the effect of squeezing the isocontour lines in the direction perpendicular to the filament and stretch them in the direction parallel to the filament. This is for example illustrated on figure 3.3.2, which shows typical mass isocontours in the HORIZON-AGN simulation (left panel) and the prediction from the constrained excursion set theory (right panel).

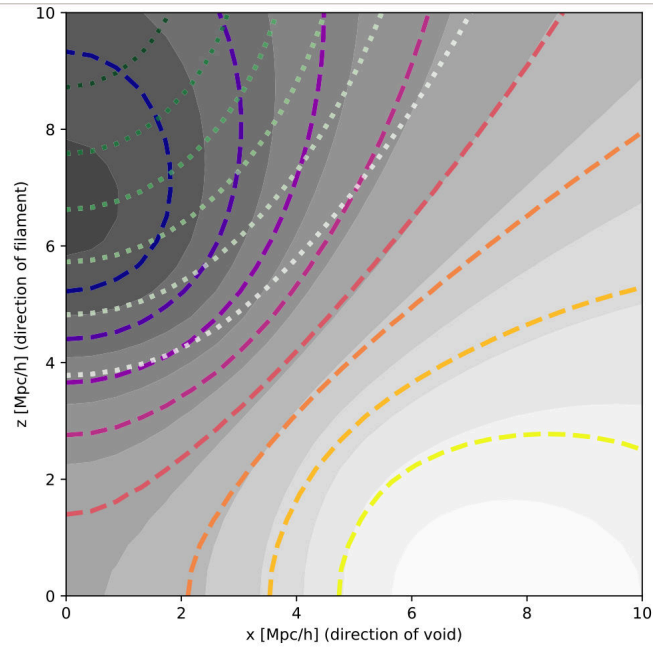


Figure 3.3.1: Isocontours of constant typical redshift $z = 0$ mean density (filled contours), mass (dotted lines) and accretion rate (dashed lines) in the frame of a filament (along the Oz axis) in Lagrangian space (initial conditions) from low (light colours) to high values (dark colours). The saddle is at coordinate $(0, 0)$ while the induced peak and void are at coordinates $(0, \pm 7)$ and $(\pm 8, 0)$ Mpc/h , respectively. The gradients of the three fields, are not parallel (the contours cross). The choice of scale sets the units on the x - and z -axis (chosen here to be $5 \text{ Mpc}/h$, while the mass and accretion rates are computed for a local smoothing of $0.5 \text{ Mpc}/h$). At lower redshift/smaller scales, one expects the non-linear convergence of the flow towards the filament to bring those contours together, as shown on figure 3.3.2.

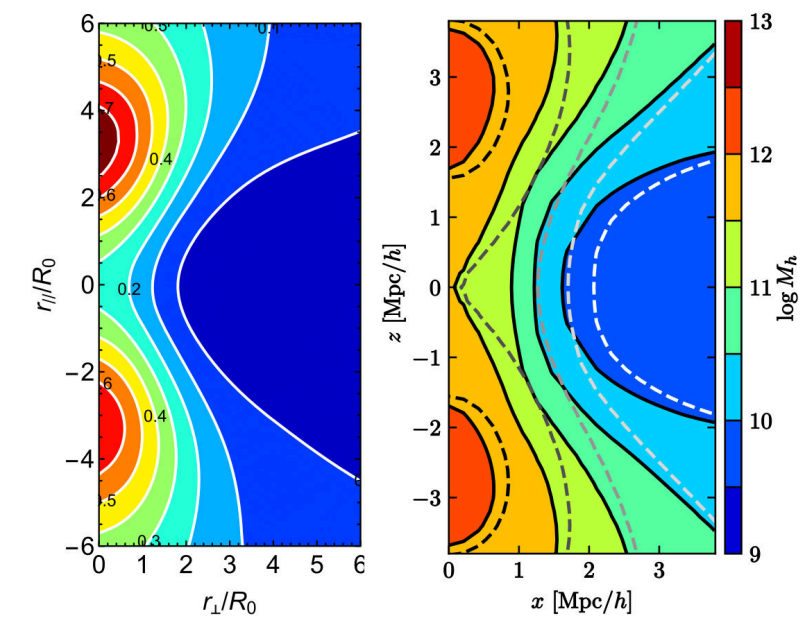


Figure 3.3.2: Typical mass measured in the HORIZON-AGN simulation (left panel, from Kraljic et al., 2019) and predictions from constrained excursion set theory (right) along the axis of filaments (vertical axis). Compared to the prediction without Zel'dovich boost (dashed lines), the isomass contour lines after the boost are compressed in the direction of filament.

4. Forecasting special events driving the assembly of dark halos

Yohan Dubois – New Horizon collaboration

Outline

4.1	Introduction	88
4.2	Theory: one-point statistics	89
4.2.1	Critical events definition	90
4.2.2	3D critical events number counts	91
4.2.3	3D differential event counts of a given height	98
4.2.4	2D event counts and differential counts	100
4.2.5	Beyond Gaussian statistics	101
4.3	Theory: two-point statistics	102
4.3.1	Clustering of critical events in R, r space	102
4.3.2	Correlation of peak merger along filament	103
4.3.3	Conditional merger rates in vicinity of larger tides	105
4.4	Measurements for Gaussian random fields	105
4.4.1	Method	105
4.4.2	Critical events counts	106
4.4.3	Two-point statistics	106
4.5	Applications to galaxy formation and discussions	109
4.5.1	Merger rates in M, z space	109
4.5.2	Consistency with cosmic connectivity evolution	110
4.5.3	Assembly bias in the frame of filaments	111
4.5.4	Departures from gaussianity	115
4.5.5	Applications beyond cosmology	119
4.6	Conclusion	119
4.A	Critical events in ND	120
4.A.1	Joint PDF of the field and its second derivatives	120

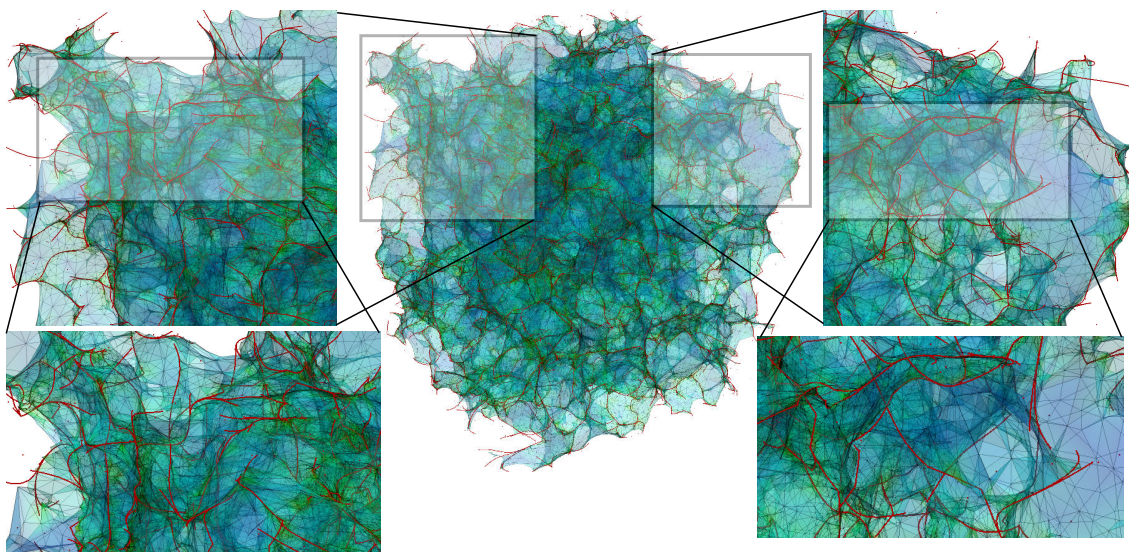


Figure 4.1.1: Snapshot and zooms of a hydrodynamical simulation showing filaments (in red) walls (in shades of blue to green) and peaks (at the nodes of the filamentary network) as traced by DISPERSE (Sousbie et al., 2011). The cosmic evolution of these large scale structures impacts the geometry of infall. As this simulation forms galaxies their properties reflect partially the corresponding tides and the funnelling of cold gas along the filamentary structure. Understanding when and how the topology of this network changes is therefore of great interest in this context.

4.A.2	Joint PDF of the first and third derivatives	120
4.A.3	Critical event number counts in ND	121
4.A.4	Ratios of critical events	122
4.A.5	Self-consistency links with critical points counts	123
4.A.6	Testing the link between critical pts and events counts	124
4.B	Algorithms	125
4.B.1	Critical points detection	125
4.B.2	Critical events detection	126
4.B.3	Generation algorithm	128
4.B.4	Comparison of two-point correlation function estimators	128
4.C	Joint PDFs	129
4.C.1	One-point PDFs	129
4.C.2	Two-point PDFs	131

4.1 Introduction

To what extent can today's properties of galaxies be predicted from the initial Gaussian random field from which they emerge? Within the paradigm of the spherical collapse, one can draw a relationship between the time of collapse of a given proto-halo given its over density, and between its mass and the scale at which its initial patch must be smoothed so as to pass a given threshold. As the halo grows in mass, it will explore larger and larger radii. In the extended Press-Schechter theory, this excursion is usually described in terms of the mean overdensity found at increasing

radii, recovering the result that large overdensities collapse earlier in cosmic time and can be further refined to take into account non-spherical collapse (e.g. R. K. Sheth et al., 2001a; Hahn et al., 2009), or the effect of gravitational clustering (Bond and Myers, 1996). In this sense, the fate of a given region is encoded in its initial conditions and is captured by the multi-scale properties of the corresponding Gaussian random field. Most of the aforementioned works have typically described proto-halos as peaks in the primordial field, effectively compressing the continuous density field into a set of points (peaks). In a more general way, the topology of the field can be described by the set of its critical points (peaks, saddle points and voids). In Hanami, 2001 it was suggested that the drift of these critical points, which draws the so-called skeleton tree, bears physical meaning, as it captures the variation of this topology with scale, hence cosmic time. In Manrique and Salvador-Sole, 1995; Manrique and Salvador-Sole, 1995; Hanami, 2001 the focus was on the coalescence of filament saddles with maxima which the authors called slopping saddles (as they are vanishing saddle points on the slope of peaks), and are proxy for halo merging events.

More generally here I will consider the coalescence of minima with wall-saddles and wall-saddles with filament-saddles corresponding respectively to the disappearance of a wall and a filament. It is the sequence and geometry of these special events in the Lagrangian patch that will later form a halo and its vicinity which will shape the fate of its host galaxy. Indeed these coalescences impact the geometry of the cosmic web (in particular the filaments) which in turn defines preferred directions along which galaxies are fed with cold gas and acquire their spin. Merger events are also known to play an important role in triggering AGN feedback, which in turn impacts gas inflow and therefore galactic morphology. Hence I will extend Hanami, 2001 by studying the clustering of these other merger events in the multi-scale landscape. The aim is to provide a compact description of the cosmic web in the initial conditions that is able to capture important events in the life of a galaxy, which includes its merger history, but also the merger history of the filaments feeding it and the merger history of the walls feeding its filaments. My motivations are many-fold:

- i) Study the generalised history of accretion: what mergers happens when, at what frequency?
- ii) Study the relation between different merger events, and their clustering in space and time,
- iii) quantify the merger rates in a larger scale filamentary structure to study assembly bias.

In order to achieve these goals, I will present the general theory of the merger events, which I will refer to as “critical events”. Section 4.2 provides a mathematical description of these events in the initial conditions and compute their one-point statistics (number counts). Section 4.3 predicts the clustering properties of these special events. Section 4.4 compares the predictions to realisations of Gaussian random fields and validates the theoretical formulas. Section 4.5 presents applications of the theory in the context of galaxy formation. Finally section 4.6 wraps up. Section 4.C presents the joint PDF of a Gaussian random field up to the third derivative of the field. Section 4.A presents the counts in arbitrary dimensions and illustrates them in up to 6D. Section 4.B explains how the critical events are measured in random field maps and cubes. Throughout the chapter, sections where the third form is used (we, us) were done in collaboration with S. Codis and C. Pichon.

4.2 Theory: one-point statistics

Let me consider the overdensity field $\delta = (\rho - \bar{\rho})/\bar{\rho}$ to be a homogeneous and isotropic Gaussian random field of zero mean, described by its power spectrum $P(k)$, as defined in section 2.1.1.3. In this section, I will focus on one-point statistics associated with merger rates. In section 4.2.1, I define the concept of critical events. In section 4.2.2, I present the number counts of critical events, counted together and by type (peak, filament and wall mergers). In section 4.2.3, I present the number counts as a function of the events' heighth. Section 4.2.4 sketches the corresponding

4.5 Applications to galaxy formation and discussions

After providing a theoretical derivation of the one-point and two-points statistics in sections 4.2 and 4.3. I have then successfully compared the predictions to Gaussian random fields and provided the two-point correlations functions in section 4.4.1.

The scope of application of the present formalism is obviously very wide. Rather than attempting to cover it all, I will present a few examples here, while a more thorough investigation is left for future work.

In a cosmic framework, section 4.5.1 will first translate the one-point statistics presented in the previous section into halo and void merger rates as a function of mass and redshift. Section 4.5.2 explains how mergers of filaments need to match that of peaks in order to preserve the connectivity of peaks. Section 4.5.3 explains how conditional merger counts in the vicinity of a filament explains how the environment drives assembly bias. Section 4.5.4 illustrates how the theoretical predictions compare to results from N -body simulations and galaxy catalogues. It also shows how wall merger rates can be used to yield constraints on modified gravity or primordial non gaussianities. Finally, applications to other fields of research in cosmology (intensity maps, weak lensing, void statistics) and beyond are discussed in section 4.5.5.

4.5.1 Merger rates in M, z space

The predictions in the initial Lagrangian space bear theoretical interest, yet they do not translate easily to measurable quantities. In this section, let me show how one can map the predictions to observable quantities, and in particular merger rates in M, z space. It is straightforward to change variable from R to M (recalling that $M = \frac{4}{3}\pi\bar{\rho}(\alpha R)^3$ from equation (4.2)) and from ν to z using the spherical collapse condition (equations 4.1 and 4.2), so that for condition c (peak, void) one has⁸

$$\begin{aligned} \frac{\partial^2 n}{\partial \log M \partial z} \Big|_c &= \frac{\partial^2 n}{\partial R \partial \nu} \Big|_c \frac{\partial R}{\partial \log M} \frac{\partial \nu}{\partial z} \\ &= - \frac{\partial^2 n}{\partial R \partial \nu} \Big|_c \frac{\delta_c}{3\alpha D(z)^2} \frac{dD}{dz} \left(\frac{3M}{4\pi\bar{\rho}} \right)^{1/3}, \end{aligned} \quad (4.39)$$

where $\alpha \approx 2.1$ and $\bar{\rho} \approx 2.8 \times 10^{11} h^2 M_\odot / \text{Mpc}^3 \Omega_M$ (see e.g. Musso et al., 2018, Table A1). The same reasoning can be applied to get a similar relation for void mergers (or equivalently wall mergers) substituting δ_c by $|\delta_v| = 2.7$ (see Jennings et al., 2013, equation 8). Note that this simple relation holds in principle for small enough voids only ($R \lesssim 3 \text{ Mpc}/h$). A more detailed study will be provided in future works. From equations (4.14) and (4.39), I am now in a position to count how many (peak, void) mergers occur early or late in the accretion history of a certain mass or within some mass range, via straightforward integration.

Figure 4.5.1 shows the merger rate of peaks and voids as a function of the mass of non linearity. The cosmology-dependant terms of equation (4.39) ($D(z)$ and dD/dz) have been computed using the code COLOSSUS (Diemer, 2018) in a Planck cosmology. With increasing time mergers of increasing size are able to happen, as the collapse barrier decreases. Note that the cutoff at large-scale is significantly faster than the Press-Schechter cutoff, as discussed below. In order to evaluate the number density of critical events, I have assumed a scale-dependant equivalent power-law power spectrum⁹.

It should in principle be possible to generalize equation (4.39) for filament mergers, but this would require the knowledge of a relation between the initial overdensity and the mass of the

⁸Note that $dD/dz = -Df/(1+z)$ with $f \equiv d \log D / d \log a \sim \Omega_m^{0.6}$.

⁹At each scale, the equivalent power-law power spectrum is given by the formula $n_{s,eq} = -3 - 2 d \log \sigma / d \log R$, where σ is computed using a Λ CDM power spectrum.

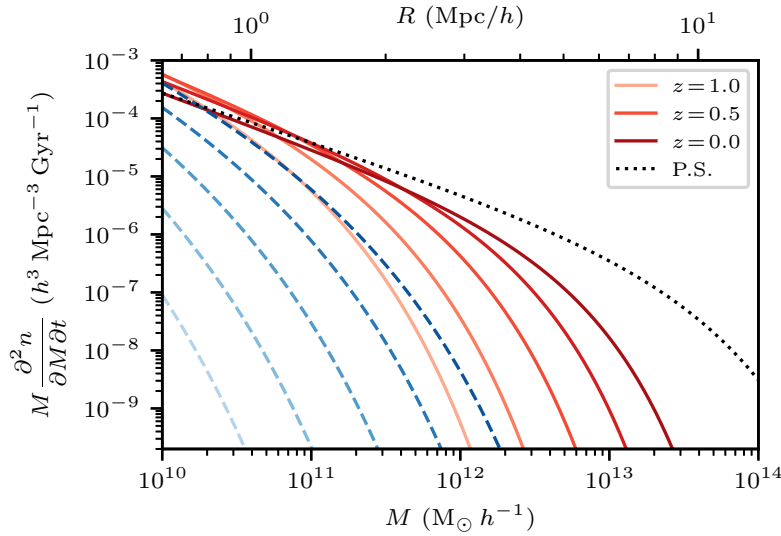


Figure 4.5.1: PDF of the halo merger rate (solid red lines) and the wall merger rate (dashed blue lines) as a function of redshift of formation (from dark to light at $z = 0, 0.25, 0.5, 0.75, 1$), see the text for details, up to a renormalisation. For the sake of clarity, only the redshifts $z = 0, 0.5, 1$ appear in the legend. For small masses the merger rate follows the Press-Schechter (Press and Schechter, 1974) halo mass function up to a renormalisation (black dotted line), while at larger masses the halo merger rate decays significantly faster. As expected, the transition mass increases with time. The same evolution is found for void mergers.

filament or its length, as well as a collapse condition. In practice, this would likely result in implementing a cylindrical collapse condition, while Pogosyan et al., 2009b suggested this could be achieved using a somehow smaller critical overdensity for filamentary collapse. The impact of our results on filament merger rates in M, z space will be done in a follow-up work.

4.5.2 Consistency with cosmic connectivity evolution

The properties of the initial random field was shown by Codis et al., 2018 to control to a large extent the connectivity of dark halos, as defined by the number of connected filaments (locally and globally) at a given cosmic time. The upshot of this work is that the packing of peaks (*i.e.* the “volume” they occupy, as imposed by their exclusion zone) and saddles implies that 3-4 filaments typically dominate locally. Interestingly, the rate of filament disappearing must match the peak merger rate, in order to preserve this number. Beyond numerology, this rate is important because filaments later feed coherently dark halos, so their their lifespan matters to understand the balance between filamentary cold gas inflow (from subsisting filaments) and environmentally-driven disruptions (from filaments mergers).

In practice, one should distinguish the local and global connectivity (see Codis et al., 2018, for more details). Unfortunately, the link between global connectivity and merger rates that was discussed in the present work does not translate straightforwardly to the local connectivity. Our qualitative understanding of the critical structure of Gaussian random fields remains in close relation to packaging: each vicinity of a critical point, and with the same argument, of a critical event, must by continuity occupy a certain volume of space, as set by its eigenvalues, which puts constraints on the position of other points in the vicinity. Indeed, critical points are found where the gradient vanishes, with some local curvature, so that the the field is quadratic in each eigenvector’s direction. As a consequence, the gradient of the field is linear at non-null separation

and cannot vanish, so that no other critical point can be found in the direct vicinity of another critical point or event. At large separations the field decorrelates from its values at the critical point, so that another critical point event becomes likely. The same reasoning applies to critical event, except that the field has a third order behaviour along the ridge of the vanishing saddle point (it is an inflexion point in that direction). The idea is that e.g. before connecting a given peak to a peak of a different height, the field must first go through a local minima along the ridge, which distance is set by the ‘width’ of that peak. For events, the process of smoothing the field will impact both the local curvature but also the curvature of these other points. Hence it is expected that smoothing jointly disconnects neighbouring peaks as mergers occur: the ridges are smoothed out because technically their saddle points vanish.

I can quantify this process via the two-point correlation functions of these events. From the auto- and cross-correlations of the \mathcal{P} and \mathcal{F} events presented in section 4.3, I can define the ratio of the separation at the maximum of these two correlations ($s_{ij} = \operatorname{argmax}_s \xi_{ij}(s)$) as a measure of the relative ‘proximity’ of the two events. Since this ratio $s_{\mathcal{P}\mathcal{F}}/s_{\mathcal{P}\mathcal{P}} \approx 3/4$ is smaller than one, it means that filament mergers are more clustered around halo mergers than halo mergers around halo mergers, so that the rate at which filaments disappear matches the merger rate and the typical number of filaments per halo remains constant through cosmic time. As a result of this spatial clustering, the most likely sequence happening is a $\mathcal{P}\mathcal{F}\mathcal{F}\mathcal{P}$, as presented on the cartoon of figure 4.5.3 in 2D. This sequence conserves the connectivity of peaks, and is consistent with the relative rates of events. Figure 4.5.4 (left panel) illustrates an analogous consistent $\mathcal{P}\mathcal{F}^4\mathcal{P}$ sequence in 3D. The right panel shows how the local connectivity of 3 can also be preserved, as the weaker filaments typically lie off the plane.

Finally, the clustering of filament disappearance impacts the connectivity of peaks as they merge as discussed in the next section, (see figure 4.5.5, bottom right panel). This is a direct consequence of the clustering of events of the various types.

4.5.3 Assembly bias in the frame of filaments

Let me now make use of the merger statistics to study the impact of the large scale structures on assembly bias, following section 4.3.3. Previous works have highlighted the modulation effect induced by large-scale filamentary structure on the assembly of dark matter halos and their galaxies. Indeed it is expected on theoretical ground that the typical accretion rate increases when going from saddle towards nodes (Musso et al., 2018). Looking at galactic properties instead, Kraljic et al., 2019 showed that the galactic ratio of rotational-velocity-to-velocity-dispersion (v/σ) is also modulated as a function of the distance and orientation to the nearest filamentary structure. Using the framework developed in this work, I generate a suite of Gaussian random fields constrained to the presence of a proto-filament at the centre of the box, the exact generation procedure being described in section 4.B.3. The proto-filament is defined at a scale $R = 5 \text{ Mpc}/h$, is oriented along the z axis and lays in a wall in the yz plane. Using the set of constrained cubes, I compute the excess density of each kind of critical event with respect to the cosmic mean, at fixed smoothing scale (hence at fixed object mass) $2.5 \leq R \leq 5 \text{ Mpc}/h$. The results are shown on figure 4.5.5.

The peak merger rate is shown on the top left panel of figure 4.5.5. Going from the voids to the wall, from the wall to the filament and from the filament to the nearest node, the peak merger rate increases and the maximum peak merger rate is found at the location where a node is expected ($z \sim \pm 10 \text{ Mpc}/h$). At larger scales, the field becomes unconstrained so that the peak merger rate falls back to its cosmic mean. I reproduce here from first principle the results of Borzyszkowski et al., 2017, showing that halos close to the filament centre are stalled compared to those in nodes: they do not undergo many mergers nor do they accrete much as the local tidal fields channels all the matter towards the two surrounding nodes, bypassing the centre of the

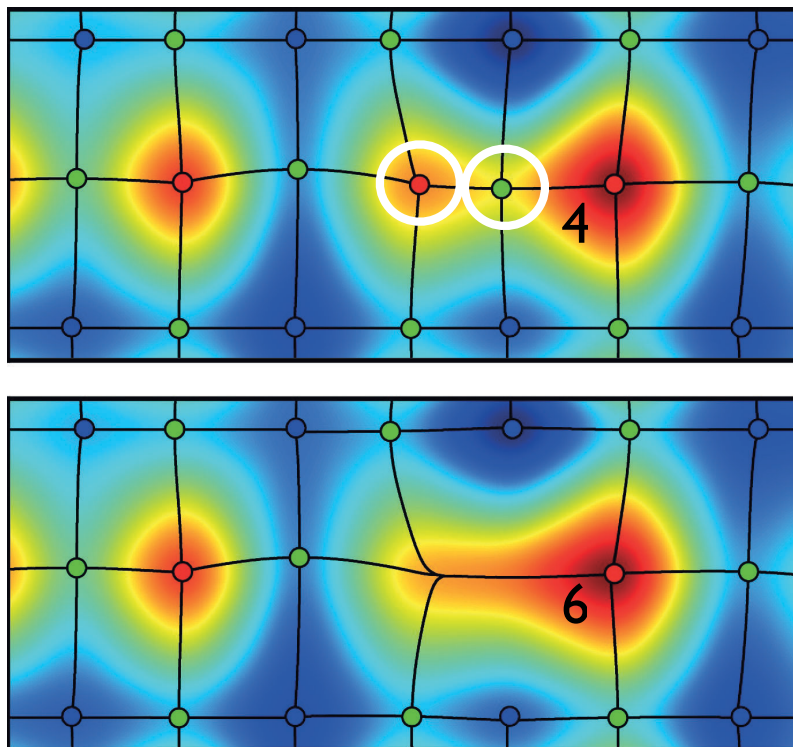


Figure 4.5.2: Snapshots of the density field at two smoothing scales (colour coded from blue, low density to red high density). The black line represents density ridges/trough connecting the red peaks, and the blue voids via the green saddle points. As the two low persistence pair of peaks (in white) merge the connectivity increases from 4 to 6 (as labeled). The fate of this connectivity now depends on the nature and location of the next merger events inspired from Sousbie et al., 2011.

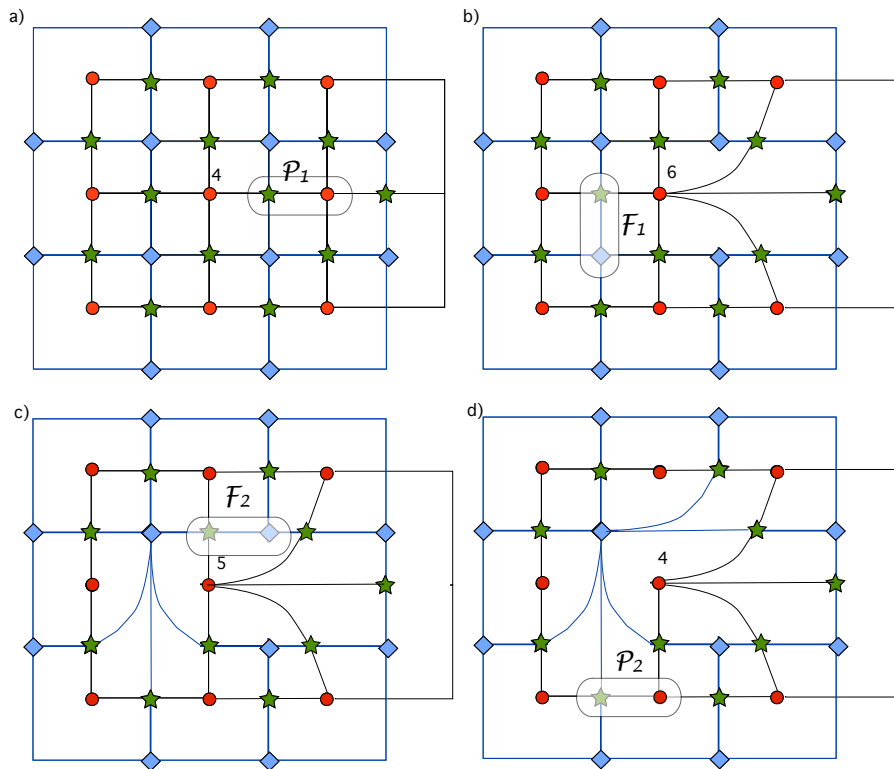


Figure 4.5.3: As labelled from a) to d) an abstraction of the merger sequence of a 2D ‘cosmic crystal’ impacting the connectivity of the central peak. Ridges are shown in black while troughs are shown in dark blue. The red circles represent the peaks, the green stars the saddles and the blue diamonds the voids. A \mathcal{P}_1 merger (highlighted in light gray) rises the mean connectivity of the central peak from 4 to 6, but the next two $\mathcal{F}_{1,2}$ mergers (highlighted in darker gray) lower it back to 4. The next \mathcal{P}_2 merger (panel d) will reduce the void’s connectivity. A more realistic representation of this process is also visible on figure 4.2.3.

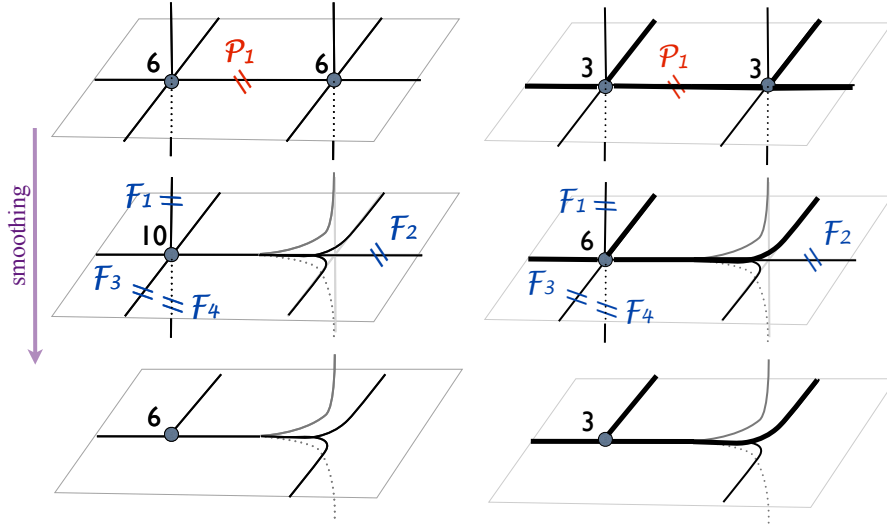


Figure 4.5.4: Following the cartoon shown in figure 4.5.3, the left panel shows a smoothing sequence (from top to bottom) which would preserve the connectivity of a 3D peak. It requires that each \mathcal{P} merger should be followed by four \mathcal{F} mergers in the vicinity. The right panel highlights how the multiplicity is preserved if one starts with 3 dominant co-planar filaments.

filament. Quantitatively, halos forming at the centre of the filament are found to have a halo merger rate close to the cosmic average, while those close to the nodes are expected to have 40% more mergers. Conversely, halos forming in a void next to a filamentary structure are expected to have a merger rate -20% smaller than the cosmic mean.

Filament merger rates act locally to decrease the connectivity of halos, as each filament merger will disconnect one filament from two halos. The top right panel of figure 4.5.5 shows that the merger rate is maximal along the wall and minimal along the filament. Going off the plane of the wall (x direction), the filament merger rate simply decreases towards the cosmic mean. Interestingly the filament merger rate is minimal in the nodes (-13%) and maximal in the wall ($+10\%$). As a consequence, halos forming close to a node have a larger halo merger rate but a smaller filament merger rate. This in turn will have an impact on the assembly of dark matter halos and their galaxies. In the wall where the filament merger rate is the highest, I expect filaments to merge faster than halos, resulting in halos with fewer connected filaments. This can be interpreted using the results of section 4.2.4. Indeed in a cosmic wall, the geometry is locally 2D so that the theoretically expected connectivity becomes 4 instead of 6.

The bottom left panel of figure 4.5.5 shows that the wall merger rate is decreased in walls and even more strongly in filaments. The minimum wall merger rate is found at the location of the node with a rate -40% smaller than the cosmic mean. Conversely, the wall merger rate is enhanced in the two voids surrounding the wall with a rate 20% above the cosmic mean.

The evolution of the connectivity with cosmic environment is resumed by the bottom right panel of figure 4.5.5, which shows the ratio of halo mergers (\mathcal{P} critical events) to filament mergers (\mathcal{F} critical events), for which the cosmic mean is 2.055 (see equation (4.17)). Small values of $r_{\mathcal{F}/\mathcal{P}}$ indicate that halo merge faster than their surrounding filaments, so that the connectivity increases as halos grow. On the contrary, large values of $r_{\mathcal{F}/\mathcal{P}}$ indicate that filaments merge faster than halos, so that the connectivity decreases as halos grow. The bottom right panel of figure 4.5.5 shows that in nodes, the ratio drops to about $r_{\mathcal{F}/\mathcal{P}} \approx 1.1$. On the contrary halos forming in voids are expected to have a ratio of about 2.4. I therefore expect that, at fixed final mass, halos forming

next to a node will grow an increasing number of connected filaments¹⁰. The expected physical outcome of this process is that the streams feeding a galaxy growing next to a node will become more and more isotropic with increasing connectivity.

Assuming that an isotropic acquisition of matter leads to a smaller amount of angular momentum being transferred down to the disk, I propose that this effect prevents the formation of gaseous disks in the vicinity of nodes. Conversely, I expect that halos growing in the neighbouring voids see their filaments destroyed faster than they merge, so that the halo is likely to grow with steadier flows coming from a few filaments (see also Codis et al., 2015; Laigle et al., 2015, section 6.2.1, and 5 resp. for similar conclusions reached via the kinematic structure of large scale flows in filaments). These effects require however a more in-depth analysis and will need to be confirmed in future works.

4.5.4 Departures from gaussianity

With increasing time, non-linearities arising from gravitational collapse translate into departures from gaussianity (Bernardeau et al., 2002). This can formally be studied in the framework described in section 4.2.5. In particular, the PDFs will become skewed as the dynamics of gravitational collapse depends on the primordial overdensity.

Results in N -body simulations

Here, let me quantify the effect first on simulations, and then compare to the proxy of section 4.2.5 relying on known perturbative results. Figure 4.5.6 presents the redshift evolution of critical counts measured in 200 realisations of Λ CDM simulations in boxes of $500 \text{ Mpc}/h$ involving 256^3 particles evolved using GADGET (Springel et al., 2001) sampled on a 256^3 grid smoothed with a Gaussian filter over $6 \text{ Mpc}/h$. The algorithm described in section 4.B is used to identify and match the critical points. The qualitative similarity with the cosmic evolution of the measured event counts and the prediction shown in figure 4.2.6 is striking, strongly suggesting that indeed, the set of critical events in the initial condition do capture the upcoming cosmic evolution of the field.

At high redshift, the Gaussian prediction is recovered. At lower redshift, the \mathcal{P} and \mathcal{F} counts shift towards lower contrast, but respectively decrease and increase in amplitude, while the \mathcal{W} counts increase in amplitude. Since the first halos to merge are due to high σ peaks, it is expected that the low- z PDFs are biased towards low densities. Similarly, the mean density of filamentary structure decreases with increasing time, as the less dense filaments take more time to gravitationally form, so that the PDFs of the filament mergers shift to smaller densities at low z . The evolution of void structures with cosmological time is somehow symmetric to the evolution of peaks: early forming voids are the most underdense while late-time voids form out of less underdense regions. At fixed resolution, this results in a shift of the typical density of voids towards higher densities. Indeed, in the limit of infinite time, it is expected that the only voids found at a given size stem from $\nu = 0$, as any void with $\nu < 0$ will have had time to collapse earlier.

Comparison to galaxy catalogues

It is of interest to follow the position of all critical points (not just the maxima) explicitly as a function of true cosmic time in galaxy catalogue extracted from hydrodynamical simulations, so as to assess i) the impact of biasing involved in selecting specific tracers and ii) how non-linear clustering impacts the statistics. This was done by N. Cornuault and C. Pichon illustratively using 330 snapshots of galaxies extracted from HORIZON-AGN (shown on figure 4.1.1 at redshift zero with its set of walls and filaments), for which the critical points are derived using DISPERSE

¹⁰Conversely Codis et al., 2015 found that when averaged over all large scale structures, connectivity increases with mass.

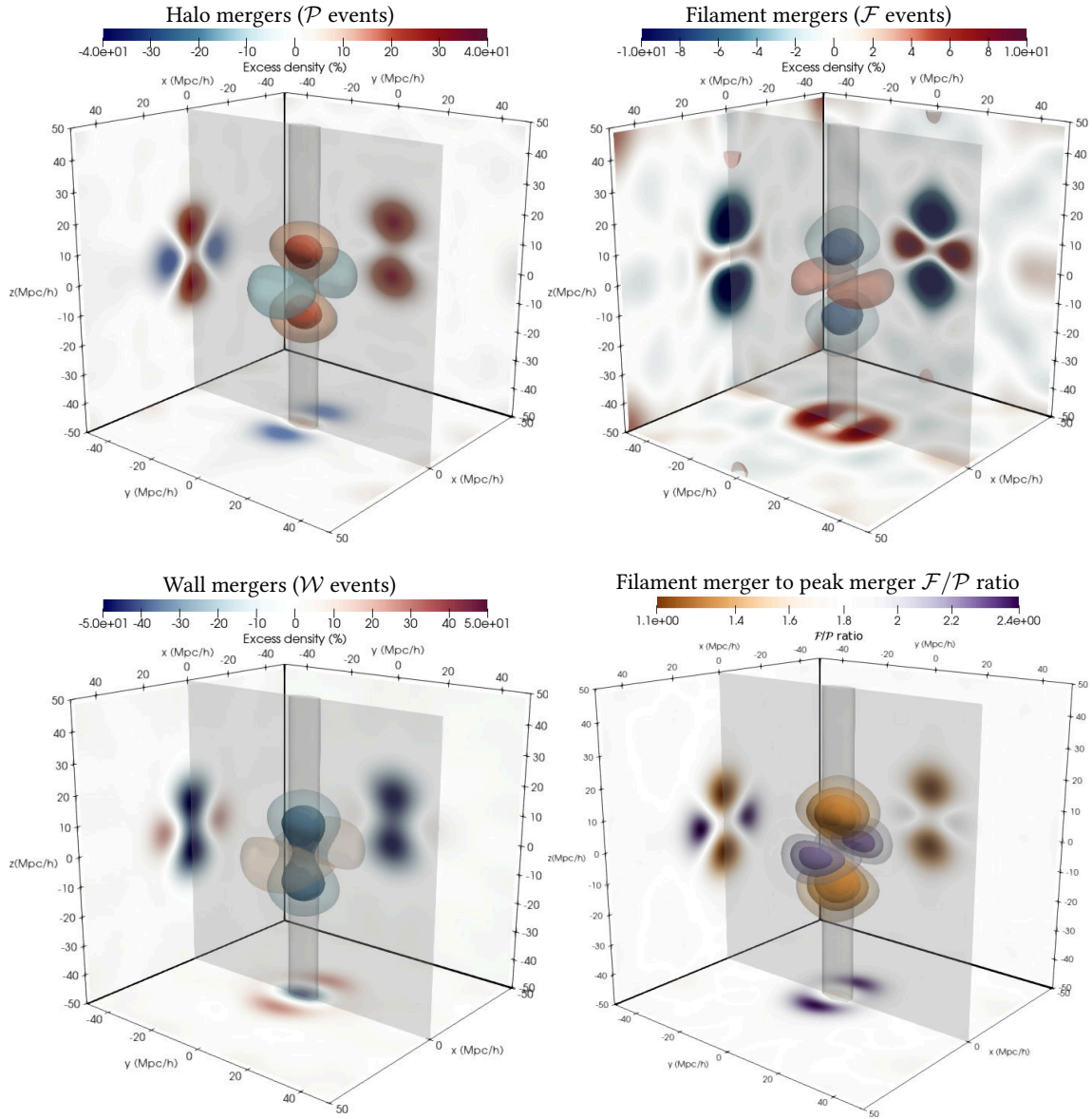


Figure 4.5.5: From left to right and top to bottom, peak-merger, filament-merger and wall-merger excess density around a large-scale proto-filament, illustrated by the vertical cylinder (z direction) and the wall in which it resides, illustrated by the grey plane (yz plane). The bottom right panel shows the local ratio of filament to peak mergers $r_{F/P}$. Each side of the cube shows a slice through the centre, shifted to the side of the plot for visualisation purposes. Red regions have an excess of critical events while blue regions have a deficit of critical events with respect to cosmic average. Interactive versions of these plots can be found online for the [halo mergers](#), [filament mergers](#), [wall mergers](#) and [filament to peak merger ratio](#). Going from voids to wall, from wall to filament and from filament to the nearest node (along the z axis), the halo merger rate increases and the filament merger rate decreases. Halos in the filament are therefore stalled: they merge less than those in the nodes. At the same time, the filament merger rate decreases when going from the filament towards the node so that the mean connectivity, given by the ratio of halo merger to filament merger, is expected to increase.

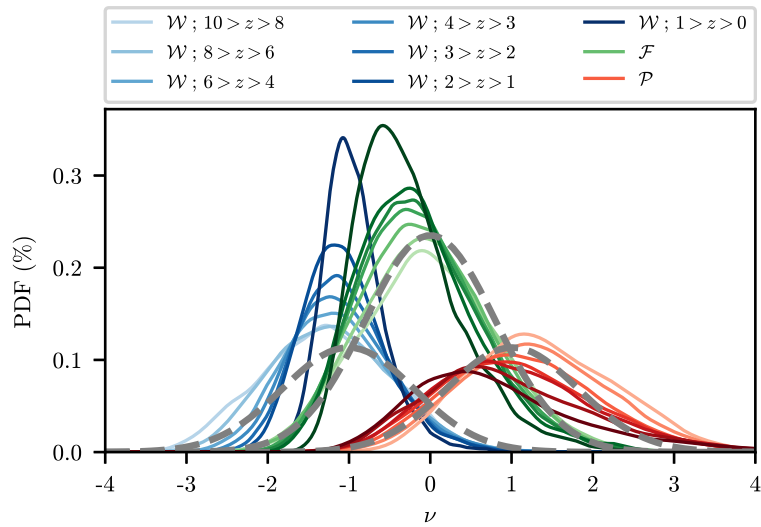


Figure 4.5.6: Critical events number count as a function of the rarity in dark-matter only simulations in different redshift bins as mentioned in the legend, with the same colours as figure 4.4.1. The curves have been normalised so that in each redshift bin, the integral of the three curves (\mathcal{W} , \mathcal{P} , \mathcal{F}) equals one. At high redshift, the merger rates resembles the Gaussian prediction (thick dashed gray lines, with an arbitrary normalisation). The skewness of the distributions increases with decreasing redshift as the field departs from gaussianity.

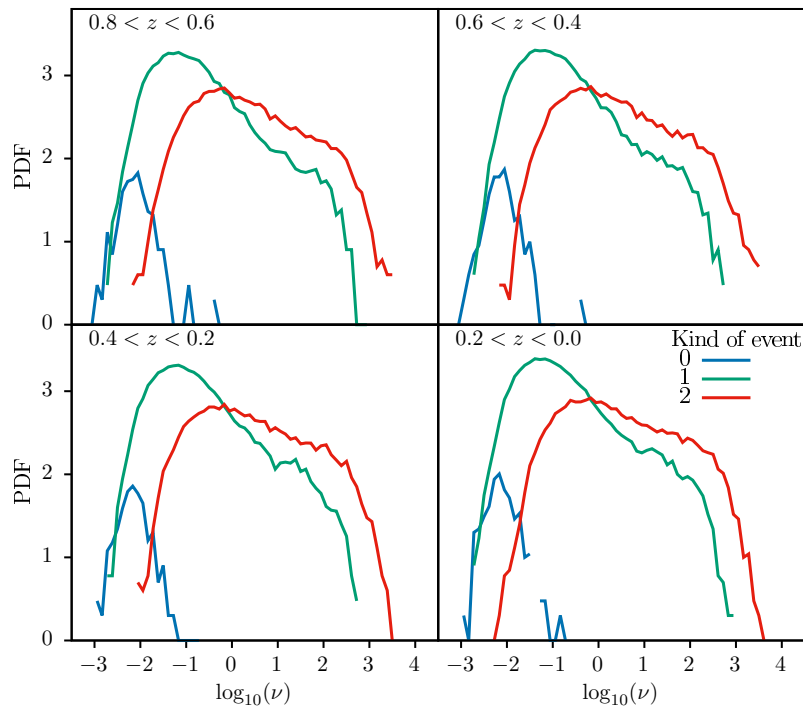


Figure 4.5.7: PDF of the critical events extracted from the galaxy catalogue of HORIZON-AGN as a function of the log galaxy density for a range of cosmic time as labelled. When compared to figure 4.5.6, the PDFs of are strongly biased, with much fewer walls hence wall mergers detected. From Nicolas Cornuault, private communications.

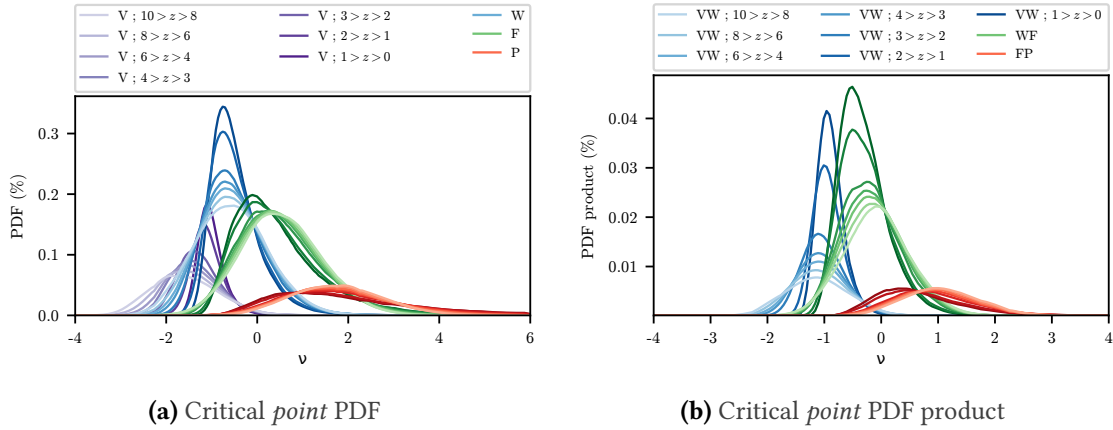


Figure 4.5.8: (a): Critical point number counts as a function of the rarity in dark-matter only simulations in different redshift bins as mentioned in the legend. The curves have been normalised so that in each redshift bin, the integral of the four curves equals one. The purple bundle corresponds to voids, the blue one to walls, the green one to filaments and the red one to peaks. (b): Product of the PDFs. At large redshifts, the curves resemble the prediction of figure 4.2.6.

with a persistence threshold of $\sigma/100$. The algorithm described in section 4.B is used to match merging critical points as a function of redshift. The set of events are then binned as a function of log density for 4 redshift bins and shown on figure 4.5.7. Gravitational clustering has skewed the PDFs, but most dramatically galaxies poorly trace under dense regions, hence the number of wall mergers plummeted. While more work needs to be done in order to be conclusive, this illustrates that the detection algorithms presented here can readily be applied to virtual catalogues in state-of-the-art simulations.

Void counts as a cosmological measurement

One particular application of these results is the study of the void number counts. Voids are very interesting laboratory both for galaxy evolution and cosmology. They represent primitive environments for galaxies, where density is low and matter flow is still relatively curl-free. Void galaxies are therefore interesting probes for galaxy formation (e.g. Lindner et al., 1996). Voids are also a tool of choice to probe the cosmology or to test theory of modified gravity (e.g. Gay et al., 2012; Lavaux and Wandelt, 2012; Cai et al., 2015) as a mean to constrain the equation of state of dark energy. In particular, these authors have used the cosmic evolution of the size and the number of voids as constrains on the linear matter growth function $D(z)$. In the present formalism void disappear as a function of cosmic time via mergers of walls, hence the one-point statistics of wall merger could be used as a cosmic probe. From equation (4.29) the cosmic evolution of the rate of void of volume \mathcal{V} merging during time interval δz can be expanded to first order in σ via equation (4.39) as

$$\frac{\partial^2 n}{\partial \log \mathcal{V} \partial z} = \frac{\partial^2 n}{\partial \log \mathcal{V} \partial z} \Big|_G + \sigma(z) \frac{\partial^2 n}{\partial \log \mathcal{V} \partial z} \Big|_{NG}, \quad (4.40)$$

where the first term reflects cosmic evolution of the rate of void disappearance presented in section 4.5.1, while the second term is obtained by substituting $\partial^2 n / \partial R \partial v \Big|_G$ by $\partial^2 n / \partial R \partial v \Big|_{NG}$ into equation (4.39). As discussed in section 4.2.5, the scaling of these non-Gaussian corrections yield joint estimates for the cumulants (Codis et al., 2013), hence a measure of f_{NL} or a parametrisation of modified gravity.

4.5.5 Applications beyond cosmology

The present analysis was mostly restricted to (quasi) Gaussian random fields, because of their relevance in cosmology and also because in this context the theory can be developed in some details. However, any system involving random field whose (continuous) evolution is controlled by one parameter could in principle be investigated with this framework in order to identify merger of ridges (though the specific role played by Gaussian smoothing would clearly generally not hold). For instance, critical events in dust maps (such as Meisner and Finkbeiner, 2014; Planck Collaboration, 2018b) could be used as an alternative statistics to quantify the properties of the underlying turbulence, a process which is known to display self similarities.

A wide range of important physical processes occur when rare events collide, hence boosting probabilities and passing thresholds, which in the context of this work corresponds to mergers of rare peaks (e.g. analysing dust map emission or disintegration events in Fermi maps). In this context, the process of interest is the appearance of pairs of critical points as one ‘unsmooths’ the field: this will correspond to the generation of pairs of critical points. Following the results of section 4.A.3, the formalism could be extended to situations where the field whose evolution is investigated corresponds to probability distributions living in higher dimensions (or on more complex manifolds).

In the context of streaming of hierarchical images the set of critical events within a 2D image characterises its multi-scale topology. It would therefore be of interest to send beforehand a description of this set as a mean of prioritising which sub region of the image needs to be streamed first because the topology of its excursion (*i.e.* the local parsimonious representation of the image as iso-contours) has changed. This would allow the received image to acquire its most important higher resolution features first.

4.6 Conclusion

As a proxy for cosmic evolution, I computed the rate of merging critical points as a function of smoothing scale from the primordial density field to forecast special events driving the assembly of dark halos and possibly galaxies. I considered all sets of critical points coalescence, including wall-saddle to filament-saddle and wall-saddle to minima, as they impact the topology of galactic infall, such as filament disconnection or void disappearance. The theory developed in this chapter, hereafter the “critical event theory”, is central to the understanding of the effect of the cosmic web on the formation of galaxies, since their evolution is the result of their past history, which is usually encoded by their merger tree and the properties of their host halo. In this context, the critical event theory provides a way to encode not only the evolution of the halo hosting the galaxy via its merger tree, but also the evolution of its upcoming internal structure with time, which itself is responsible for driving the angular momentum acquisition, as will be seen in chapter 6. I argue that the theory can be seen as an extension to the classical halo model, where the properties of galaxies have an extra dependence on their “dressed” merger history which takes into account the merger history of their surrounding filaments and walls.

The scope of this theory is obviously very broad, but let me sum up here the results relevant to astrophysics and in particular to the problem of the assembly of galaxies.

- I studied critical events of all types, their clustering properties, and presented analytical formulae for the one-point statistics of these events in fields of dimensions up to 6, and also the two-point statistics.
- I have established the link between critical events and connectivity. This allows me to compute the connectivity of peak and other critical events in arbitrary dimensions. Physically, I established the duality between the evolution of the cosmic web (critical events) and its topological features (connectivity).

- I provided a covariant formulation of the critical event theory which allowed me to also compute the two-point statistics for critical events. The two-point statistics show that halo mergers are typically followed by a filament merger, so that the connectivity is conserved.
- I have shown that the critical event theory can be further extended to take into account the early stages of non-linear gravitational evolution. This has then been compared positively to numerical simulations at high redshift. This extension also probes the non-Gaussianities that arise from primordial non-Gaussianities and can be used as a cosmological measurement.
- I showed how one can use critical events as an input to galaxy formation models, and in particular as input to machine learning techniques. I also presented how this framework could be wired to a Bayesian inference model to compute the amount of information brought by the critical event, and eventually answer the question of which galactic properties are driven by the cosmic web.
- I have shown that halos forming in nodes grow by successive mergers, while their filaments do not merge, so that their local connectivity increases. The trend is expected to reverse in voids, where filament mergers happen faster than halo mergers, resulting in halos with a small connectivity. This is likely to have an impact on galaxy formation, and in particular on angular momentum acquisition.

I have only touched on practical applications for the forecasting of special events in a multi-scale landscape. It should prove to be a fruitful field of research in astronomy and beyond in the future.

This work is part of an on-going research effort and will lead to a publication in the near future.

4.A Critical events in ND

For the sake of completeness and possible interest in other fields of research, let us present the one-point statistics of critical events in arbitrary dimension d .

4.A.1 Joint PDF of the field and its second derivatives

From Pogosyan et al., 2009b the probability of measuring the set of d eigenvalues of the d dimensional Hessian $\{\lambda_i\}$ and density ν obeys

$$\mathcal{V}_d \prod_{i \leq d} d\lambda_i \prod_{i < j} (\lambda_j - \lambda_i) \exp\left(-\frac{1}{2}Q_\gamma(\nu, \{\lambda_i\})\right), \quad (4.41)$$

where Q_γ is a quadratic form in λ_i and ν given by

$$Q_\gamma(\nu, \{\lambda_i\}) = \nu^2 + \frac{(\sum_i \lambda_i + \gamma\nu)^2}{(1 - \gamma^2)} + \mathcal{Q}_d(\{\lambda_i\}), \quad (4.42)$$

with

$$\mathcal{Q}_d(\{\lambda_i\}) = (d + 2) \left[\frac{1}{2}(d - 1) \sum_i \lambda_i^2 - \sum_{i \neq j} \lambda_i \lambda_j \right]. \quad (4.43)$$

In equation (4.41) \mathcal{V}_d arises from the integration over the angles and is given by equation (4.56) below.

4.A.2 Joint PDF of the first and third derivatives

Here, we will look into the PDF of the first and third derivatives in d dimensions in order to compute the odd derivative term C_{odd} that enters critical event number counts in d dimensions.

First, let us note that the first derivatives are Gaussian distributed with individual variance $\langle x_i^2 \rangle = 1/d$ so that the probability for all first derivatives to be zero is

$$P(\nabla\rho = 0) = \left(\frac{d}{2\pi}\right)^{d/2}. \quad (4.44)$$

Now let us study the statistics of the third derivatives. By symmetry, one can note that

$$\left\langle \left(\sum_i x_{1ii} \right)^2 \right\rangle = \frac{1}{d}, \quad (4.45)$$

because the third derivatives are rescaled by σ_3 , and

$$\langle x_{1jj}^2 \rangle = \langle x_{111}x_{1jj} \rangle = \frac{1}{5} \langle x_{111}^2 \rangle = 3 \langle x_{1jj}x_{1kk} \rangle \quad \forall j \neq k \neq 1.$$

Therefore,

$$\frac{1}{d} = \langle x_{111}^2 \rangle + (d-1) \langle x_{1jj}^2 \rangle + 2(d-1) \langle x_{111}x_{1jj} \rangle + (d-1)(d-2) \langle x_{1kk}x_{1jj} \rangle \quad \forall j \neq k \neq 1 \quad (4.46)$$

implies that $\langle x_{iii}^2 \rangle = 15/d(d+2)(d+4)$ and the full covariance matrix of the third derivatives is therefore now known. However, we are interested in statistics subject to a zero gradient constraint, in particular the three quantities of interest are (fixing d as the degenerate direction and assuming an implicit summation on the i indices)

$$\langle x_{ddd}^2 | x_d = 0 \rangle = \langle x_{ddd}^2 \rangle - \frac{\langle x_{dii}x_d \rangle^2}{\langle x_d^2 \rangle}, \quad (4.47)$$

$$\langle (x_{dii})^2 | x_d = 0 \rangle = \langle (x_{dii})^2 \rangle - \frac{\langle x_{ddd}x_d \rangle^2}{\langle x_d^2 \rangle}, \quad (4.48)$$

$$\langle x_{dii}x_{ddd} | x_d = 0 \rangle = \langle x_{dii}x_{ddd} \rangle - \frac{\langle x_d x_{ddd} \rangle \langle x_d x_{dii} \rangle}{\langle x_d^2 \rangle}, \quad (4.49)$$

which can easily be computed thanks to the additional relation $\langle x_{11}^2 \rangle = 3/d(d+2)$,

$$\langle x_{ddd}^2 | x_d = 0 \rangle = \frac{3}{d(d+2)} \left[\frac{5}{d+4} - \frac{3\tilde{\gamma}^2}{d+2} \right], \quad (4.50)$$

$$\langle (x_{dii})^2 | x_d = 0 \rangle = \frac{1 - \tilde{\gamma}^2}{d}, \quad (4.51)$$

$$\langle x_{dii}x_{ddd} | x_d = 0 \rangle = \frac{3}{d(d+2)} (1 - \tilde{\gamma}^2). \quad (4.52)$$

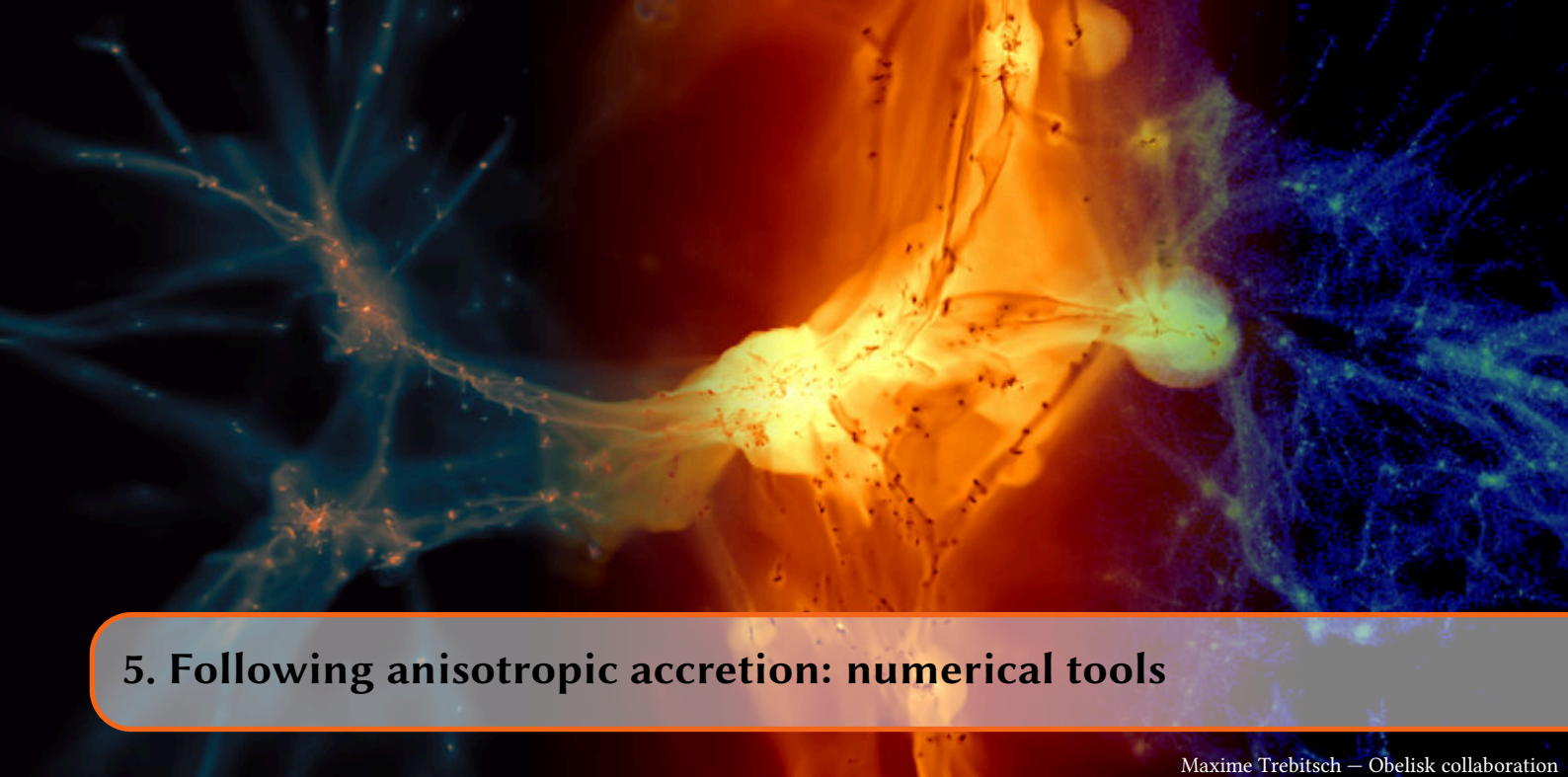
4.A.3 Critical event number counts in ND

It now follows that the critical event number counts of type j at height ν in dimension d read

$$\frac{\partial^2 n_j^d}{\partial R \partial \nu} = \frac{R \mathcal{V}_d C_{d,\text{odd}}}{\tilde{R}^2 R_*^d} \left\langle \delta_D(\lambda_j) \left| \prod_{i \neq j \leq d} \vartheta_H(\lambda_i - \lambda_j) \lambda_i \right. \right\rangle, \quad (4.53)$$

where this expectation is computed using the conditional expectations presented in the previous section. Equation (4.53) is a function of ν because of the correlation between ν and $\sum_i \lambda_i$ seen in equation (4.42). Recalling the formal analogy with the flux of critical lines per unit hyper surface,

$$\frac{\partial^2 n_p^d}{\partial R \partial \nu} \underset{\gamma \nu \rightarrow \infty}{\sim} \frac{R}{\tilde{R}^2 R_*^d} \frac{\mathcal{V}_d C_{d,\text{odd}}}{\sqrt{2\pi}} \exp \left[-\frac{1}{2} \nu^2 \right] \left(\frac{\nu}{R_0} \right)^{d-1},$$



5. Following anisotropic accretion: numerical tools

Maxime Trebitsch — Obelisk collaboration

Outline

5.1	Introduction	133
5.2	“Accurate tracer particles of baryon dynamics in the adaptive mesh refinement code Ramses”	134
5.3	Torque extraction	152
5.3.1	Gravitational torques	152
5.3.2	Pressure gradient estimation	153
5.4	Conclusion	157

5.1 Introduction

Astrophysical numerical codes usually solve the equation of hydrodynamics in two different approaches, following either the Lagrangian or Eulerian description of the gas. In the former approach known as SPH, the basic elements are macro-particles that represent a given mass of gas (Springel et al., 2001; Wadsley et al., 2004; Price et al., 2017). This approach very conveniently provides the Lagrangian history of the gas, as each particle carries a fixed amount of mass along with their thermodynamical quantities (temperature, density, velocity, metallicity). Another possible approach known as AMR is based on a Eulerian point of view. In these methods, the basic elements are finite volumes of gas (Teyssier, 2002; Bryan et al., 2014), spatially laid on a grid. One of the strength of AMR methods is their ability to control the spatial resolution in regions of interest by adapting the resolution. The most common approach is the so-called “pseudo-Lagrangian” refinement scheme, where regions containing a lot of mass are refined, effectively ending up with each volume containing a similar mass. One can however trigger refinement on

arbitrary criterion, such as the gas vorticity, the local Jeans length or above a certain pressure gradient, so that the geometry of the flow can be captured by adapting the geometry of the grid. As AMR methods are built around Riemann solvers, they are also very good at capturing shocks in numerical simulations. They can therefore provide a very good solution to the problem of cosmic accretion, which requires to accurately resolve shocks around the virial radius. However, due to their Eulerian nature, AMR codes are unable to capture the Lagrangian evolution of the gas and do not provide the past thermodynamical history of a parcel of gas.

This caveat is particularly problematic when studying cosmic accretion, and in particular cold flows as their peculiar evolution is usually captured by their maximum temperature, as the gas that composes them never heated up above a given threshold (see section 6.2.3) This effectively selects the gas that crossed the virial radius without shocking, so that the definition of cold flows requires the knowledge of the past Lagrangian history of the gas. To overcome this issue, AMR codes have been equipped with “tracer” particles. Tracer particles are passively displaced with the gas flow and hence track its Lagrangian evolution. On their trajectory, they usually record instantaneous quantities, in particular the temperature of the gas and its density, but also the torques resulting from the gravitational interaction of the gas with the halo and the disk and from the pressure of the surrounding hot medium.

This chapter presents a technical description of the tools I developed in order to make RAMSES suited to the study of cold flows, although the methods presented hereafter can also be applied to a variety of other problems. Section 5.2 presents a new tracer particle scheme developed for the code RAMSES. I compare the implementation to previous ones and show that it largely improves the results. In particular, the new tracer particles are able to accurately reproduce the Eulerian distribution of the gas (so that they are trustable) and also provide the entire Lagrangian evolution of the gas (so that they provide a comprehensive history of the gas evolution). Section 5.3 presents the methods developed to compute the different torques acting on a parcel of fluid in post-processing. As will be shown in the next chapter, these methods can then be used to provide a detailed description of the evolution of the angular momentum of the cold flows.

5.2 “Accurate tracer particles of baryon dynamics in the adaptive mesh refinement code Ramses”

One of the requirements of tracer particles is that they should accurately reproduce the Eulerian distribution of the gas. In the naive approach, tracer particles are advected by the gas by interpolating the velocity. This is usually done with a cloud-in-cell interpolation (first order interpolation), where the value of the velocity is interpolated from the 8 closest cells. Such a velocity-based approach was implemented in RAMSES (Dubois et al., 2012) and used to probe the link between cosmic gas infall and galactic gas feeding. This approach yields smooth Lagrangian trajectories, yet it falls short of reproducing the gas density distribution accurately in regions of converging flows, as I showed in Cadiou et al., 2019 (paper below). In addition, there is no natural way of taking into account transfers of baryons between the gas, stars and SMBHs which are particularly relevant in the context of galaxy formation in the inner regions surrounding the galaxy.

Using a different approach, Genel et al., 2013 suggested to instead sample mass fluxes *via* a Monte-Carlo method. In this approach, the mass flux between cells, which is readily computed by the Riemann solver of the code, is approximated by moving particles across cells interface: each particle jumps from cell i to cell j with probability

$$p_{ij} = \frac{\Delta M_{ij}}{M_i}, \quad (5.1)$$

where ΔM_{ij} is the transferred mass (as computed by the Riemann solver) and M_i is the mass

of the cell originally containing the particle. Since tracer particles reproduce mass fluxes, their evolution is fully consistent with that of the gas, up to a sampling noise.

Instead of providing smooth trajectories, Monte Carlo tracer particles provide a statistical sample whose mean accurately tracks the properties of baryons in the simulation and whose spatial distribution matches the Eulerian gas density. They are therefore perfectly suited to the problem of cold filamentary accretion. In the paper provided hereafter, I present the details of the implementation for gas-to-gas transfers. I then present how one can extend equation (5.1) to take into account any baryon transfers, providing a clear improvement over previous tracer particle implementations. I then show that my implementation is able to accurately reproduce the Eulerian distribution of the gas, while providing at the same time the full Lagrangian evolution of baryons in their journey in the gas, stars and SMBHs. As a proof of concept, the method is then applied to the problem of cold flows to recover the bimodal accretion mode observed in SPH simulations (e.g. Kereš et al., 2005).

The paper, published in A&A in Cadiou et al., 2019, is provided hereafter.

5.3 Torque extraction

Most of the previous works (Danovich et al., 2015; Prieto et al., 2017) have studied the relative contribution of each torques to the angular momentum (AM) evolution of the cold gas focusing in particular on their magnitude, splitting the torques between the pressure and the gravitational torques. This section provides an improvement over these past works by computing the gravitational torques from each sources (stars, DM and the gas) separately. I also lay down a general method to compute gradients in post-processing in AMR codes, which I then use to compute pressure gradient, and in particular, pressure torques. The precise computation of pressure gradients and the component-by-component decomposition of the gravitational torques will prove important in the context of the study of the evolution of cold flows in galaxies, as will be discussed in more depth in chapter 6, but let me first present here how one can rigorously compute them.

Section 5.3.1 details the method I developed to compute the gravitational torques from the different sources in numerical simulations. I show that I am able to extract the torques originating from the DM, stars, the gas. The method is then checked and I show that it provides percent-accurate results. Section 5.3.2 details the method I developed to compute the pressure torques in post-processing. The method can be used in general to compute any spatial derivative on an AMR grid that can be computed from the values of the direct neighbours, which includes the gradient, the divergence, the curl and the laplacian operators.

5.3.1 Gravitational torques

In the vicinity of galaxies, the different massive sources (DM, stars, gas) all contribute to the total gravitational potential $\phi = \phi_{\text{DM}} + \phi_{\star} + \phi_{\text{gas}}$ via the Poisson equation

$$\nabla^2 \phi_i = 4\pi G \rho_i, \quad (5.2)$$

where ϕ_i and ρ_i are the gravitational potential and the density of the component i (DM, stars, gas). One can then compute the specific forces resulting from each potential $\mathbf{F}_i = -\nabla \phi_i$ which can then be used to compute the specific torques at position \mathbf{r}

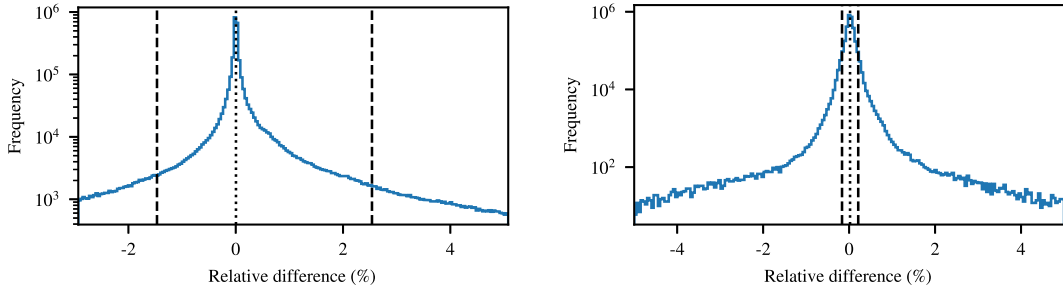
$$\boldsymbol{\tau}_i \equiv \mathbf{r} \times \mathbf{F}_i. \quad (5.3)$$

In order to extract the torques resulting from each gravitational source, I have modified the code RAMSES to extract in post-processing the specific forces due to the different matter components (DM, gas, stars). This was performed by stripping down RAMSES to keep only the Poisson solver, applied to the density of each individual component¹. Since the resulting code is a simplified version of RAMSES, it can be run with exactly the same parameters as the original run, so that the results yielded are consistent (for example, the cosmology is the same). Using the numerical simulation detailed in section 5.2, I have computed the gravitational force of the stars, gas and dark matter that act on the gas for each output. For each component (star, gas and DM), I have also computed the rate of change of specific angular momentum (sAM) of the gas as

$$f_i = \frac{\boldsymbol{\tau}_i \cdot \mathbf{l}}{\|\mathbf{l}\|^2}, \quad (5.4)$$

where $\mathbf{l} = \mathbf{r} \times \mathbf{v}$ is the gas sAM, both positions and velocities are evaluated for the gas in the frame of the central halo. Note that equation (5.4) yields a quantity that can be interpreted as the number of time torques are able to remove all the AM per unit time (it is a frequency). Equation (5.4) is therefore a measure of the inverse e-folding time along the Lagrangian trajectory of a particle. f_i is positive and large where torques are efficient at increasing the sAM and negative where

¹The fiducial implementation solves the Poisson equation directly on the total matter density (gas + stars + DM).



(a) Error on evolution rate computation

(b) Error on acceleration computation

Figure 5.3.1: (a): Relative difference between the sum of the sAM evolution rate due to stars, DM and gas gravitational forces (as computed with the method presented in the text) and the rate due the total gravitational torques (as computed by RAMSES). (b): Same, but with the total gravitational accelerations. Vertical dashed line indicate 5 % and 95 % quantiles. The vertical dotted line indicates the median value. The two methods yield similar results within a few percent.

torques are efficient at decreasing the sAM. Figure 5.3.1a shows the relative difference between the sum of the evolution rates $f_{\star} + f_{\text{DM}} + f_{\text{gas}}$ extracted individually in post-processing and the total evolution rate $f = \boldsymbol{\tau} \cdot \boldsymbol{l} / \|\boldsymbol{l}\|^2$ computed on-the-fly by RAMSES. Figure 5.3.1b shows the relative difference between the gravitational accelerations computed using the two methods. The agreement is of the order of less than a percent in 90% of the cells. Note that a perfect agreement is not expected, as the potential from the SMBHs has been neglected in the post-processing method. In addition, RAMSES' Poisson solver has an intrinsic accuracy of 10^{-4} , consistent with the median error obtained in the gravitational accelerations (0.02 %). Overall, the agreement between the computed rates are within a few percent. The errors on the evolution rate are slightly larger, albeit still small, as a result of the division by l that skews the distribution and spreads assigns larger weights in regions where l is small. This confirms that the post-processing decomposition yields results consistent with the on-the-fly-computed gravitational field used internally to evolve the simulation.

5.3.2 Pressure gradient estimation

The precise capture of shocks is fundamental to most of the astrophysical codes. These shocks then result in strong, short-wavelengths gradients which are usually captured by a few cells in most AMR codes. While numerical codes routinely deal with strong gradients, most AMR post-processing tools either do not provide any utility to compute them (pynbody, Pontzen et al., 2013, pymsses Guillet et al., 2013), or have gradient computing capacities that are not available for octtree-based AMR datasets, as is the case with RAMSES, (e.g. yt Turk et al., 2011). The approach usually followed is to project data on a fixed resolution grid, which is then used to compute gradients using a finite-difference scheme. Even though this approach yields sensible results at scales comparable to the (arbitrary) grid spacing, any information at finer scales is smoothed out while values at coarser levels have to be interpolated, eventually leading to spurious gradients. In the case of the study of accretion onto galaxies, the fixed-grid approach fails to provide a precise description of the gradients at play (pressure and potential gradients), as shocks may form anywhere in a large volume $\sim R_{\text{vir}}^3$. In order to capture all shocks on a regular grid, one would then require the grid to be at least as well-resolved as the AMR grid, effectively requiring

$\sim (R_{\text{vir}}/\Delta x)^3 \approx (100 \text{ kpc}/30 \text{ pc})^3 \approx 3 \times 10^{10}$ cells.² This is in practice too large to fit in memory, as it would require about 120 Gio of data as each pixel requires 40 of data. In practice, it is much more efficient *and* consistent to directly work on the AMR structure dumped alongside the physical information of the simulation.

Using a tree search algorithm, as illustrated on figure 5.3.3, I have developed a post-processing tool that is able to compute finite difference gradients directly on the AMR grid. The binary search algorithm ensures that any given location is found in at most N steps, where N is the number of AMR levels in the simulation (typically between 10 and 20). To do so, I have extended the yt code (Turk et al., 2011) to enable computation of gradients for oct-based AMR datasets. The algorithm works as follow. (a) Loop over all octs in the tree. (b) Compute the positions of the $4^3 = 64$ virtual cells centred on the oct and extending in $\pm 2\Delta x$ in all three directions, as illustrated on figure 5.3.2, left panel. (c) Get the value of interest at the centre of each virtual cell from the AMR grid. If the virtual cell exists on the grid or is contained in a coarser cell, the value on the grid is directly used. If the virtual cell contains leaf cells, the mean of these cells is used.³ (d) Compute the gradient of the quantity using a centred finite-difference scheme on the 4^3 grid, as illustrated on figure 5.3.2, right panel. (e) Store the value of the gradient in the central 2^3 cells.

This approach aims to provide results as close as possible to the values used internally by RAMSES. It is worth noting that this approach is exactly consistent with the internal approach of RAMSES, except at the interface between different grid levels where a linear interpolation is used by RAMSES, whereas our method uses a simple average. One way to check the consistency is to compare gradients computed by the post-processing tool to the ones computed internally by RAMSES. This is for example done using the velocity divergence, as shown on figure 5.3.4. The figure shows that the post-processing method recovers the velocity divergence within a few percent, while most of the scatter is attributed to the fact that RAMSES uses a linear interpolation at the interface between coarse and fine cells.

²Here I have used the resolution of the simulation presented in section 5.2 and the typical size of the virial radius of a $10^{12} M_{\odot}$ halo at $z = 2$.

³Note that to be fully consistent with RAMSES at fine-to-coarse boundaries, one should either use a linear interpolation with a total variation diminishing scheme (TVD) or a straight injection and use $1.5\Delta x$ distance in the gradient estimate.

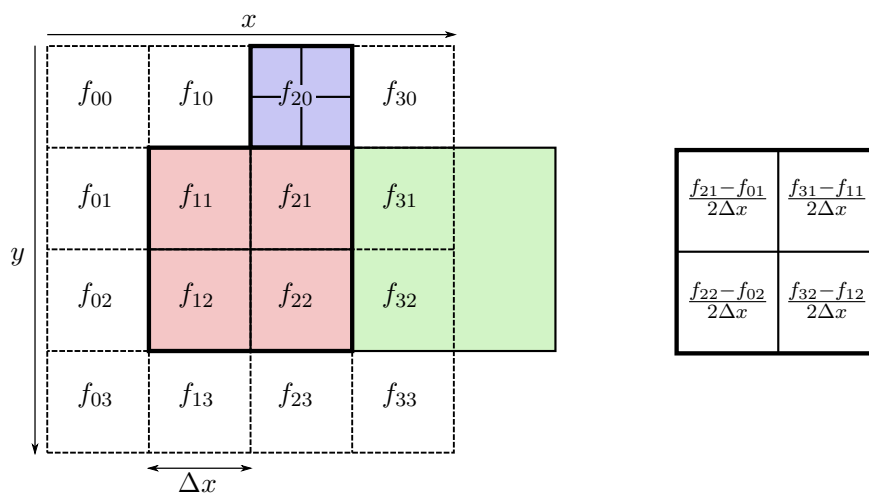


Figure 5.3.2: Scheme of the AMR structure used to estimate the gradient of a quantity f in the central oct (red). Octs are represented in thick lines, cells in thin lines and virtual cells in dashed lines. *Left panel:* The virtual cell values on a 4^3 grid are interpolated from the nearest cell in the AMR grid. If the nearest cell is at the same level, its value is directly used. If the cell is at a coarser level, its value is directly used (for example f_{31} and f_{32} have the value of the green cell). If the cell is refined, the mean of its children is used (for example f_{20} is the mean of all the blue cells). *Right panel:* Gradients are estimated using a first-order finite difference centred scheme on the 4^3 virtual cells.

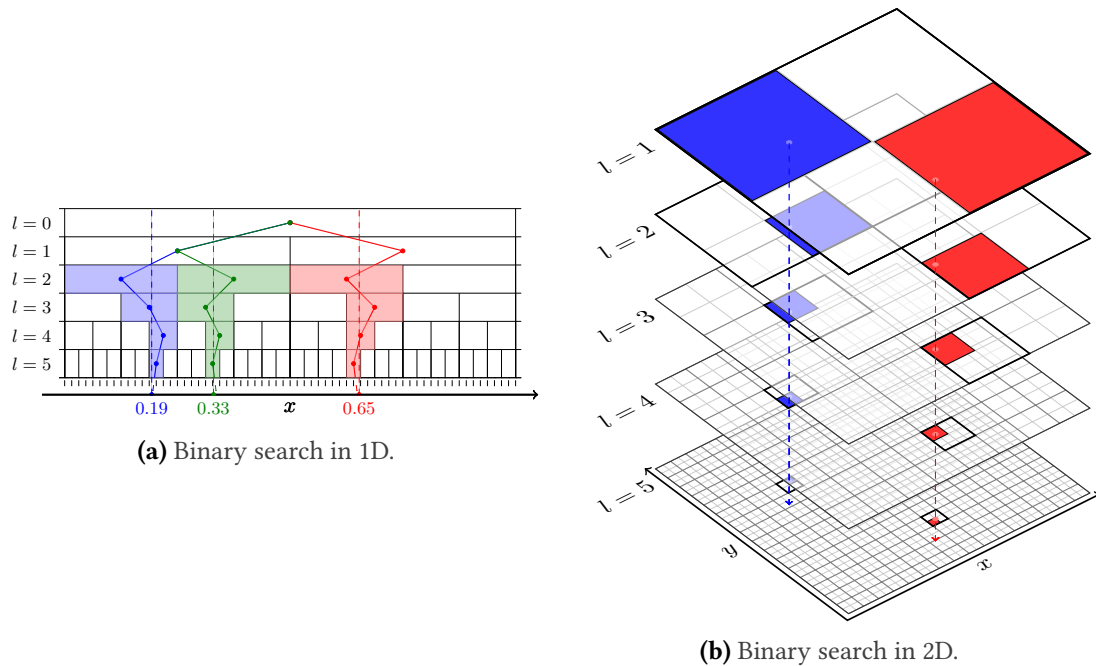


Figure 5.3.3: (a) Scheme of a binary search in an oct structure in 1D. The requested points are shown as red and blue dashed lines. The algorithm starts at the root level $l = 0$ and goes down the structure ; at each level, it picks the cell that contains the requested point. (b) A similar illustration in 2D, the algorithm works in the same way. At each level, it selects one of the four cells (red and blue squares) from the oct (thick line). The algorithm can be easily generalised to three or more dimensions. It is able to find any cell containing a given point in l_{\max} iterations exactly. If the grid is sparse, as is the case for an AMR structure, l_{\max} becomes an upper boundary.

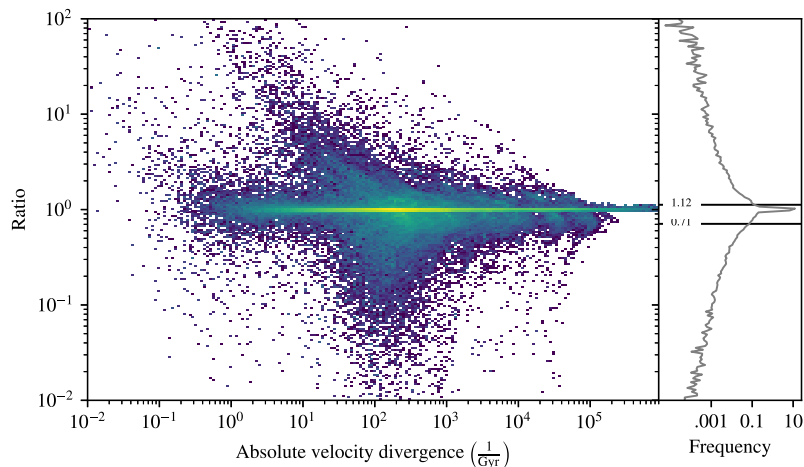


Figure 5.3.4: *Left panel:* Plot of the velocity divergence as computed by RAMSES vs. the ratio of the value computed in post-processing to RAMSES's one. *Right panel:* PDF of the ratio. 95 % of the distribution falls between the two horizontal lines. 95 % of the cells have a value between 0.71 and 1.12 times the value computed internally by RAMSES.

5.4 Conclusion

In section 5.2, I have presented a new tracer particle scheme. I have shown that it is able to accurately capture the Lagrangian evolution of the baryons in a full-featured cosmological simulation. In particular, I showed that the tracer particles have a spatial distribution close to that of the gas, which significantly improves over previous methods. I also showed that the tracer particles can be used to get the full Lagrangian evolution of the baryons as they move from gas to stars and into SMBHs. In section 5.3, I presented two numerical methods to extract the torques acting on a parcel of fluid. The methods presented have been shown to yield consistent results that are much improved compared to previous methods. The gravitational torque extraction method can be used to decompose the contribution to the gravitational torques due to each individual components (DM, stars and gas). I have also presented a method to compute pressure gradients on an AMR grid which I then applied to the computation of pressure torques. This approach provides results consistent with the internal values of the code.

The methods detailed in this chapter have a broad range of application. The tracer particle scheme has already been adopted by other researchers to study the formation and destruction of clumps in clusters (see appendix B.3) and to study gas flows in the circumgalactic medium (P. Mitchell, private communications). They are also used in the context of protoplanetary disk formation, where they have been modified to follow the Lagrangian evolution of dust grains (U. Lebreuilly, private communications). The gradient computation was for example used to compare the cosmic ray pressure gradient, thermal pressure gradient and gravitational acceleration in isolated simulations of dwarf galaxies, and concluded that cosmic ray pressure was the dominant acceleration mechanism above 1 kpc from the plane of the disc (G. Dashyan et al., submitted).

A visualization of the cosmic web, showing a complex network of filaments and nodes. The central region is bright yellow and orange, while the outer filaments are blue and purple. The background is dark, making the glowing structures stand out.

6. Angular momentum acquisition from the cosmic web

Maxime Trebitsch — Obelisk collaboration

Outline

6.1	Introduction	160
6.2	Methods	162
6.2.1	Equations	162
6.2.2	Numerical simulation	163
6.2.3	Cold gas selection	164
6.3	Results	167
6.3.1	Specific angular momentum vs. angular momentum per unit volume	167
6.3.2	Dominant forces in the cold and hot phase	167
6.3.3	The magnitude of the angular momentum	168
6.3.4	The orientation of the angular momentum	169
6.3.5	Dominant torques in the cold and hot phase	171
6.4	Discussion	174
6.5	Conclusion	178
6.A	Additional material	179
7.1	Closing remarks	183
7.2	Perspectives and applications of my work	186
7.2.1	Extensions of the constrained excursion set theory	186
7.2.2	Following dust formation using Monte-Carlo sampling methods	187
7.2.3	Critical events as input to Machine learning and Bayesian inference	187

6.1 Introduction

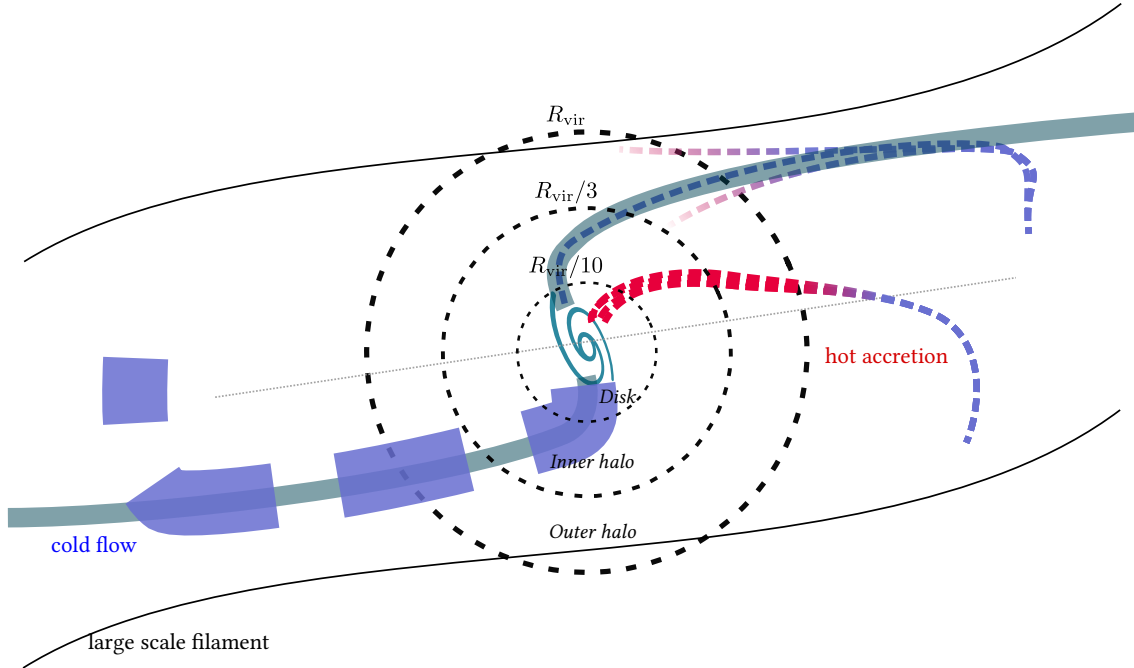


Figure 6.1.1: Sketch of the galaxy and its environment with the outer halo ($r > R_{\text{vir}}/3$), the inner halo ($R_{\text{vir}}/3 > r > R_{\text{vir}}/10$) and the disk ($r < R_{\text{vir}}/10$). The mode of accretion are the cold mode via cold flows (in blue) and the hot mode, characterized by a stable shock at the virial radius (in red). Cold flows may also shock and heat at a smaller radius to be determined. On large scales, cold flows are embedded in the cosmic web.

One of the successes of the Λ CDM model is its ability to reproduce the large-scale structure of the Universe observed in galaxy distribution (e.g. Springel et al., 2006). These structures form out of the initial tiny density fluctuations of the primordial density field and under the effect of gravitational forces, matter departs from underdense regions to flow through cosmic sheets into filamentary structures. Matter then flows from these filaments towards high-density peaks that will later become halos. In the process, matter acquires properties (e.g. vorticity Pichon and Bernardeau, 1999; Laigle et al., 2015) in its journey through voids, sheets and filaments of the cosmic web, which, in turn, affect the assembly of dark matter halos, as shown in chapter 4. Baryons follow the same initial fate as DM and flow from underdense regions to sheets. Yet, as they flow in sheets, pressure forces prevent them from shell-crossing so that they lose their normal velocity component to the shock front, dissipating large-scale acquired kinetic energy into internal energy (eventually radiated away by gas cooling processes). Following potential wells created by dark matter, baryons then flow towards filamentary structures where they lose a second component of their velocity¹ and reach a dense-enough state to efficiently cool radiatively.

At first order, galaxy formation is affected by the mass of their dark matter halo host and the local environment, as encoded by the local density on sub-Mpc scales, as it is assumed that baryons have the same past accretion history as dark matter. These models have proven successful at explaining a number of observed trends, in particular against isotropic statistics, in the so-called halo model, yet they fail at explaining some effects such as spin alignments (Tempel and Libeskind, 2013; Codis et al., 2015; Dubois et al., 2014; Chisari et al., 2017), colour segregation (Laigle et al.,

¹The component lost is in the direction perpendicular to the shock, which is in the plane of the wall and the filament.

2018; Kraljic et al., 2018; Kraljic et al., 2019) or star formation rates (Malavasi et al., 2017; Kraljic et al., 2019). Indeed, galaxies form by converting their gas into stars and by successive mergers, which are in turn affected by the tides and large-scale modulations of the density field induced by the cosmic web. The detailed history of how the gas was acquired and how much AM it brought, as well as the origin of the mergers should in principle impact the formation of the galaxy. Since the physical processes involved in dark matter halos formation differ from the baryonic processes at the core of galaxy formation, one can expect that the cosmic web will have a different impact, if any, on the formation of galaxies and may explain the disparity of their properties in similar-looking dark matter halos.

In particular, at fixed halo mass and local density, properties of galaxies such as their colour or the kinematic structure vary with their location in the cosmic web. One key process in the differential evolution of galaxies is gas accretion. Indeed, at large redshifts it has been suggested that the accretion of gas is dominated by flows of cold gas funnelled from the large scales to galactic scales (Birnboim and Dekel, 2003; Dekel and Birnboim, 2006). This mode of accretion has then been confirmed in numerical simulations using different methods (Kereš et al., 2005; Dekel and Birnboim, 2006; Ocvirk et al., 2008; Nelson et al., 2013) as the source of a significant fraction of the baryonic mass but also AM (Pichon et al., 2011; Kimm et al., 2011; Tillson et al., 2015; Stewart et al., 2017) and it has been proposed that these flows may feed supermassive black holes (Di Matteo et al., 2012; Dubois et al., 2012), which in turn affect the cold inflow rates (Dubois et al., 2013). Using an extension of TTT (Peebles, 1969; Schaefer, 2009), Codis et al., 2015 showed that anisotropic environments, such as large-scale filamentary structures, biases the AM distribution to align it with the cosmic web. It is then expected that this gas will fall in galaxies *via* cold flows, feeding disks with angular-momentum rich gas that is itself aligned with the tides of the cosmic web.

Recent works have shown that the flows are subject to a variety of processes: they may fragment (Cornuault et al., 2018) or be disrupted by hydrodynamical instabilities (Mandelker et al., 2016; Mandelker et al., 2019) but they are also sensible to feedback events (Dubois et al., 2013). In this context, Danovich et al., 2015 showed that in numerical simulations, cold flows are nevertheless able to feed galaxies with angular-momentum rich material (as speculated by Pichon et al., 2011; Stewart et al., 2013). In this study, it was shown that the AM acquired outside the halo at $z = 2$ is transported down to the inner halo; the gas then settles in a ring surrounding the disk, where gravitational torques spin the gas down to the mean spin of the baryons. Another study, albeit at larger redshifts, found that the dominant force was pressure (Prieto et al., 2017). Since there is not much freedom on the final AM of the galaxies, as constrained by their radius, the excess AM brought by cold flows has to be redistributed somehow before it reaches the disk. The details of where this AM will end up are key to understand the AM distribution in galaxies, but also to understand to what extent their spin is aligned with the cosmic web. If the dominant forces acting on the AM are pressure forces, resulting from internal processes (SN winds, AGN feedback bubbles), then the spin of the galaxy would likely be a result of chaotic internal processes and would lose its connection to the cosmic web. Similarly, if the AM is lost into thermal energy (which is then radiated away) in shocks, the galactic spin would be a weak function of the large-scale AM induced by the cosmic web. On the contrary, if the dominant forces are gravitational forces, then the spin-down of the cold gas is likely to drive a spin-up of either the disk or the dark matter halo, which themselves are the result of their past AM accretion history. In this last scenario, the details of which part(s) of the halo or the disk interact exchange AM with the infalling material would constrain models aimed to understand the evolution of the spin of galaxies.

Historically, the study of cold accretion has been particularly challenging in numerical simulations. Early simulations using SPH methods largely over-estimated the fraction of gas accreted cold (see e.g. Nelson et al., 2013, for a discussion on this particular issue) as a result of the

difficulty to capture shocks using SPH. AMR simulations do not suffer from this caveat (Ocvirk et al., 2008), yet they fail at providing the Lagrangian history of the gas – in particular its past temperature – which is required to detect the cold-accreted gas. In order to circumvent this limitation, most simulations relied on velocity-advected tracer particles (Dubois et al., 2013; Tillson et al., 2015). However, this approach yields a very biased tracer distribution that fails at reproducing correctly the spatial distribution of gas in filaments: most tracer particles end up in convergent regions (center of galaxies, center of filaments) while divergent regions are under-sampled. In order to reproduce more accurately the gas distribution, Genel et al., 2013 suggested to rely on a Monte-Carlo approach where tracer particle follow mass fluxes instead of being advected. Using this approach, I have showed in chapter 5 (Cadiou et al., 2019) that tracer particles are able to faithfully reproduce the gas distribution while providing the Lagrangian history of the gas, and in particular its past temperature and position.

In this chapter, I detail the results obtained from cosmological simulations of group progenitors as $z > 2$. I provide a detailed study of the evolution of the AM of the cold and hot gas. In particular, this chapter aims at answering the question of which forces are responsible for the spin-down and realignment of the AM of the gas accreted in the two modes of accretion (hot and cold). Section 6.2 presents the numerical setup. Section 6.3 presents a detailed study of the AM evolution of the cold and hot gas. It details the evolution of the magnitude and orientation of the AM and the different forces and torques at play in the different regions of the halos. Section 6.4, I discuss the results and their implication on the distribution of AM in the galaxy and the inner halo. Finally, section 6.5 wraps things up and concludes.

In the following of this chapter, I will adopt the same naming conventions as Danovich et al., 2015. I will write R_{vir} the virial radius of a halo. The outer halo is defined as the region between R_{vir} and $R_{\text{vir}}/3$. The inner halo is defined as the region between $R_{\text{vir}}/3$ and $R_{\text{vir}}/10$. The “disk” is the region at radius $r < R_{\text{vir}}/10$ where the galaxy is found. This is sketched on figure 6.1.1.

6.2 Methods

In this section, I detail the equations used throughout the remaining of the paper. In section 6.2.1, I establish the equations that link the AM evolution of the gas to the different torques. In section 6.2.2, I describe the simulations I ran. In section 6.2.3, I describe how I selected the cold gas being accreted on the halos in the simulations.

6.2.1 Equations

I first derive the equation driving the evolution of the sAM of the gas, In the following, the position and velocities are computed in the frame of halo, as measured with the ADAPTAHOP halo finder (Tweed et al., 2009).

$$\mathbf{l} = \mathbf{r} \times \mathbf{v}. \quad (6.1)$$

To do so, let us start from Euler’s equation and the mass conservation equation

$$\frac{\partial \rho}{\partial t} + \nabla \cdot (\rho \mathbf{v}) = 0, \quad (6.2)$$

$$\frac{\partial \mathbf{v}}{\partial t} + (\mathbf{v} \cdot \nabla) \mathbf{v} = -\frac{\nabla P}{\rho} - \nabla \phi. \quad (6.3)$$

Taking the derivative of equation (6.1) w.r.t. time, one gets that

$$\frac{d\mathbf{l}}{dt} = \mathbf{r} \times \left(\frac{\partial \mathbf{v}}{\partial t} + (\mathbf{v} \cdot \nabla) \mathbf{v} \right) + \left(\frac{\partial \mathbf{r}}{\partial t} + (\mathbf{v} \cdot \nabla) \mathbf{r} \right) \times \mathbf{v}. \quad (6.4)$$

After trivial algebra, the rightmost part of the right hand side vanishes. Using equations (6.3) and (6.4), the Lagrangian time derivative of the sAM then reads

$$\frac{d\mathbf{l}}{dt} = \boldsymbol{\tau}_P + \boldsymbol{\tau}_\phi, \quad (6.5)$$

where $\boldsymbol{\tau}_P \equiv -\mathbf{r} \times \nabla P/\rho$, $\boldsymbol{\tau}_\phi = -\mathbf{r} \times \nabla\phi$ are the specific pressure and gravitational torques. Here P and ρ are the pressure and density of the gas and ϕ is the gravitational potential. The potential is defined using Poisson equation

$$\nabla^2\phi = 4\pi G\rho_{\text{tot}}, \quad (6.6)$$

where ρ_{tot} is the total matter density (DM, stars, gas and SMBHs). Using the linearity of equation (6.6), the total potential can be written as the sum of the potential due to each component $\phi = \phi_{\text{DM}} + \phi_\star + \phi_{\text{gas}}$ ². One can similarly decompose the gravitational torques into three different components $\boldsymbol{\tau}_\phi = \boldsymbol{\tau}_{\phi,\text{DM}} + \boldsymbol{\tau}_{\phi,\star} + \boldsymbol{\tau}_{\phi,\text{gas}}$. In the following, I will use this decomposition to assess which gravitational components contributes to the evolution of the sAM of the gas.

Following section 5.3, let me define the rate of change induced by each torque

$$f_i = \frac{\boldsymbol{\tau}_i \cdot \mathbf{l}}{\|\mathbf{l}\|^2}, \quad (6.7)$$

where i indicates the torque source (DM, star or gas gravitational torques or pressure torques). I have shown in the previous chapter that this quantity has the physical meaning of the inverse e-folding time of the sAM on a Lagrangian trajectory. Using equation (6.5) and after some algebra, one also gets that the total rate of change can be simply expressed as the variation of the sAM $f = d \log l / dt$. Let me emphasize here that this relation only holds for the total rate of change. From equation (6.7), one can also define a typical timescale associated with the torques as

$$t_{\tau,i} = \left| \frac{1}{f_i} \right|. \quad (6.8)$$

These timescales measure the typical time over which a given torque will significantly change the sAM of the gas. As equations (6.7) and (6.8) only use the contribution of the torque in the direction of the sAM, the timescale measures the typical time required to loose all the sAM, but not to reorient it. Note that one could compute similarly the re-alignment timescale by replacing the dot product of equation (6.7) with the norm of the cross product $f_{\perp,i} \propto |\boldsymbol{\tau}_i \times \mathbf{l}|$. In addition, the timescale and the rate of change are scalars that can have a negative value if the torques are spinning the gas down (anti-aligned with the sAM vector) while it has a positive value if they are spinning the gas up (aligned with the sAM vector).

6.2.2 Numerical simulation

I have run a suite of three 50 cMpc/h-wide cosmological simulations, hereafter named S1, S2, S3. The three simulations contain 6 halos with $M \gtrsim 5 \times 10^{11} M_\odot$ ³, hereafter named A, B, C, D, E and F. Their properties are presented in Table 6.1. The size of the zoomed Lagrangian volume in the initial conditions is chosen to encapsulate twice the virial radius of the halo at $z = 2$. The simulation are started with a coarse grid of 128^3 (level 7) and several nested grids with increasing levels of refinement up to level 11. The adopted cosmology has a total matter density of $\Omega_m = 0.3089$, a dark energy density of $\Omega_\Lambda = 0.6911$, a baryonic mass density of $\Omega_b = 0.0486$, a Hubble constant of $H_0 = 67.74 \text{ km s}^{-1} \text{ Mpc}^{-1}$, a variance at 8 Mpc $\sigma_8 = 0.8159$, and a non-linear power spectrum index of $n_s = 0.9667$, compatible with a Planck 2015 cosmology (Planck Collaboration, 2015).

²Here I neglect the contribution from SMBHs as it is negligible on galactic scales.

³Only pure halos in the zoomed-region have been selected.

Figure 6.3.8 shows that, once averaged over the entire cold phase, pressure forces do not contribute significantly to the variation of the sAM of the gas. Indeed, I have shown on figure 6.3.7 that pressure forces are dominated by high-frequency spatial modulations, with a signal-to-noise ratio of the order of 10^{-3} . While the magnitude of the pressure forces are comparable to the DM gravitational forces, their net contribution to the torque budget is shown to be at least three order of magnitude smaller. As gas falls towards the galaxy, gravitational forces exert increasing torques resulting in a spin-down of the gas. In the inner halo down, torques become weakly aligned to the mean sAM of the gas at R_{vir} , so that their projection can either contribute to the spin-up or spin-down in this specific frame, which is shown on figure 6.3.8 by rapid jumps from negative to positive values. Similar results can be found if one projects the torques on the axis of the AM vector of the galaxy at the end of the simulation, $L_{\star}(z = 2)$, as shown for halos A and B on figure 6.A.2. These plots also feature individual Lagrangian trajectories of the gas and illustrate that pressure torques spin the gas up as much as they spin it down. In contrast, gravitational torques are coherent over the Lagrangian evolution of the gas, so that their contribution adds up to spin the cold gas down. The bottom-right panels of figure 6.A.2 show the ratio of the DM gravitational torques to the stellar gravitational torques. As shown in figure 6.3.8, stellar gravitational torques are negligible in the outer halo but become dominant in the inner halo and in the disk.

The hierarchy between the different torques can in principle evolve with redshift. In order to study their relative importance, I have computed the total pressure torques, DM gravitational torques and stellar torques and compared the magnitude of each torques to the total torques from all sources $\tau_{\text{all}} = \tau_{\text{P}} + \tau_{\text{DM}} + \tau_{\star}$. The ratio r is then defined as

$$r_i = \frac{|\sum_{\text{particles}} \tau_i|}{|\sum_{\text{particles}} \tau_{\text{all}}|}. \quad (6.11)$$

Here i can be any of P, DM, \star and sums run over all cold gas particles. The results are presented on figure 6.3.9, where torque ratios are presented as a function of the radial distance to the galaxy. Note that due to the the definition, ratios can exceed one⁴. The figure shows that after a settling time of about 1 Gyr ($z = 5.7$), the ratios of each torques are constant at all radii, with the DM gravitational torques dominating in the outer halo and stellar gravitational torques dominating around the disk. Outside the halo at $2R_{\text{vir}}$, the gravitational torques contribute to 90% of the total torques, while this fraction decreases to about 60% at $R_{\text{vir}}/3$. In the disk, gravitational torques are dominated by stellar gravitational torques. In the six halos, the net contribution of pressure torques is negligible.

6.4 Discussion

At large radii, the evolution of the AM follows the tides imposed by the cosmic web, as explained by the TTT (e.g. Codis et al., 2012). The gas then flows on the forming galaxy *via* two different channels: the hot and cold accretion, in particular for massive enough galaxies at $z \gtrsim 2$ (Birnboim and Dekel, 2003; Dekel and Birnboim, 2006; Pichon et al., 2011; Nelson et al., 2013). The predominance of one or the other channels of accretion can be used to understand the formation of disky galaxies and the internal evolution of the galaxy. Indeed, in cold flows that result from cold accretion, the gas is able to penetrate deep in the halo and can feed the galaxy with fresh gas, with a steady AM orientation (Pichon et al., 2011; Danovich et al., 2015). In numerical simulations, it has however been observed that cold gas has a higher AM at larger radii, as measured by their spin parameter (Kimm et al., 2011; Tillson et al., 2015; Danovich et al., 2015) which is up to one order of magnitude larger than that of the DM. In the inner halo and the disk however, the

⁴This can happen if two torques have similar magnitudes but opposite directions.

spin parameter of the cold-accreted gas is found to be only three times larger than that of the DM at the same location. The nature of the torques acting to reduce the AM of the gas is still debated today. While Danovich et al., 2015 argued that the dominant torques are gravitational torques regardless of the distance to the galaxy, Prieto et al., 2017 instead found that the dominant torques were pressure torques. In this work, I find that the pressure forces are dominant in the hot phase and are as important as the DM gravitational forces in the outer halo, in particular in the ortho-radial direction. In the inner halo, a transition occurs so that the dominant forces become stellar gravitational forces. I also report a significant “pressure ring” in the inner halo that may affect the kinematics of the infalling gas in which pressure forces dominate over all forces in both the cold- and hot-accreted gas. This pressure ring may have significant implications on the thermodynamical evolution of the gas, as well as to contribute to mixing the cold-accreted material to the hot gas, effectively blurring the line between hot- and cold-accreted material. The study of this pressure ring will be the topic of future work.

While pressure forces can act locally as the dominant forces, I report that their net contribution to the evolution of the cold gas is negligible. Indeed, pressure forces do not possess any structure over hundreds of parsecs, so that their individual contribution to the evolution of the cold gas cancel out. On the contrary, gravitational forces, that depend on the distribution of matter on larger scales, are able to coherently apply torques on the infalling material, resulting in most of the spin-down signal.

The net effect of the gravitational forces is reported to be a spin-down of the accreted gas, as a result of dynamical friction and gravitational torques. Most of the spin-down of the hot gas happens before entering the halo and is due to DM torques. One possible reason for this is the following: under the effect of gas infall, the DM halo becomes slightly polarised which in turn creates a tidal field that will torque the hot gas down. Using the ortho-radial gravitational forces reported in figure 6.3.1, the typical angular momentum of the gas upon its entry in the halo ($\sim 10^4$ km/s kpc) would be depleted in a time $t_{\text{torque}}(R = 100 \text{ kpc}) = |l|/|\tau| \approx 10^4 \text{ km/s kpc} / 10^{-1} \text{ km/s/Myr} \times 80 \text{ kpc} \approx 1250 \text{ Gyr}$, which is about twice the free-fall time of the halo $t_{\text{ff}}(z = 2) = 500 \text{ Myr}$ at $z = 2$. If the hot gas lingers in the outskirts of the outer halo during two free-fall times, the DM gravitational torques are large enough to get rid of most of the angular momentum before accretion. In our simulations, hot gas takes on average $(1000 \pm 500) \text{ Myr}$ to fall from $3R_{\text{vir}}(z = 2)$ to $R_{\text{vir}}(z = 2)/3$ where $R_{\text{vir}}(z = 2)$ is the final virial radius of the halo at $z = 2$.

Interestingly, I find that, even though most of the AM has been lost before entering the halo, the orientation of the AM of the hot gas is well-conserved between R_{vir} and $R_{\text{vir}}/3$. This can be explained either by the fact that the spin of the halo, which has been reported to be well aligned with the first principal axis of the large scale tides (Danovich et al., 2012) do not reorient significantly the AM of hot gas, or that the infall of the hot gas coincides with the loss of most, but not all, of its angular momentum. In this scenario, the hot gas starts infalling at the sweet spot where most of the angular momentum has been lost, but before all of it has been removed.

As reported in Rosdahl and Blaizot, 2012, the trajectory of the cold gas is different and follows a mostly radial (with a non-null impact parameters) free-fall trajectory. In our simulation, the cold gas typically takes $(500 \pm 350) \text{ Myr}$ to go from $3R_{\text{vir}}$ to $R_{\text{vir}}/3$, so that the halo gravitational torques are not large enough to reduce the AM of the cold gas. As the cold gas plunges into the halo, the influence of the disk increases up to the point where torques become dominated by stars. I report here that the location where the disk torques become important coincides to the location where most of the AM of the cold gas has been lost. This may be an indication that the disk is actually responsible to the spin-down of the cold gas. If so, one would need to understand how the disk responds to an anisotropic accretion and more work is needed to understand in details the origin of the torques originating from the disk. One can then suggest that both the inner halo

and the disk will then tend to be aligned to the mean orientation of the inflowing material in a similar way. This may explain why galactic spin is well aligned with the internal halo's, while being only mildly aligned with the global halo spin.

Cornuault et al., 2018 suggested that cold flows do not survive within the halo. They suggested that they instead fragment into clouds while their internal pressure increases. In the process, the kinetic energy of the gas is lowered as part of it is converted into turbulence and the gas mixes much more efficiently with the hot gas of the halo, effectively losing the shielding effect usually assumed for cold flows. In this scenario, the pressure gradients observed in my simulations may contribute to efficiently mix the angular-momentum rich cold gas to the hot gas. This would likely result to a diffusion of the AM of the cold gas into the hot medium and increase the relative importance of pressure torques to the problem of the AM transport.

Using idealised simulations, Mandelker et al., 2016; Padnos et al., 2018; Mandelker et al., 2019 showed that cold flows may also be sensitive to the Kelvin-Helmholtz instability. In particular, they showed that thin-enough filaments are destroyed before reaching the galaxy. In this last case, the cold gas would effectively lose its angular momentum to the hot halo before interacting with the galaxy. Interestingly, these studies also suggested that cold flows may entrain the neighbouring hot gas as they fall in while slowing down the infall of the cold gas, which may result in an efficient mixing of the AM at the boundary of the cold flows. Berlok and Pfrommer, 2019 suggested that the mixing may be decreased if one considers magnetised flows with field lines parallel to the flow, as a the result of a magnetic tension working against the Kelvin-Helmholtz instability.

Nelson et al., 2015 studied the effect of AGN feedback on cold accretion. They showed that feedback is able to significantly increase the infall time. If the delay is large enough, DM gravitational torques may have time to remove all AM from the cold gas before it enters the inner halo – as is already the case with hot gas in the simulations presented in this dissertation. In another study on the effect of AGN feedback on cold flows, Dubois et al., 2013 showed that at $z \geq 6$, the AGN activity in massive halo is able to prevent cold flows from reaching the disk and significantly decreases the cold gas mass in the inner halo. On large scales, AGN activity increases the curvature of filaments and decreases their length. The exact effect of AGN feedback will require further studies. It may lead to a revision of the results presented in this dissertation depending on their ability to disrupt the cold flow structures prior to accretion and delay the infall. One possible way to study this would require to run numerical simulations with different AGN feedback strengths.

6.5 Conclusion

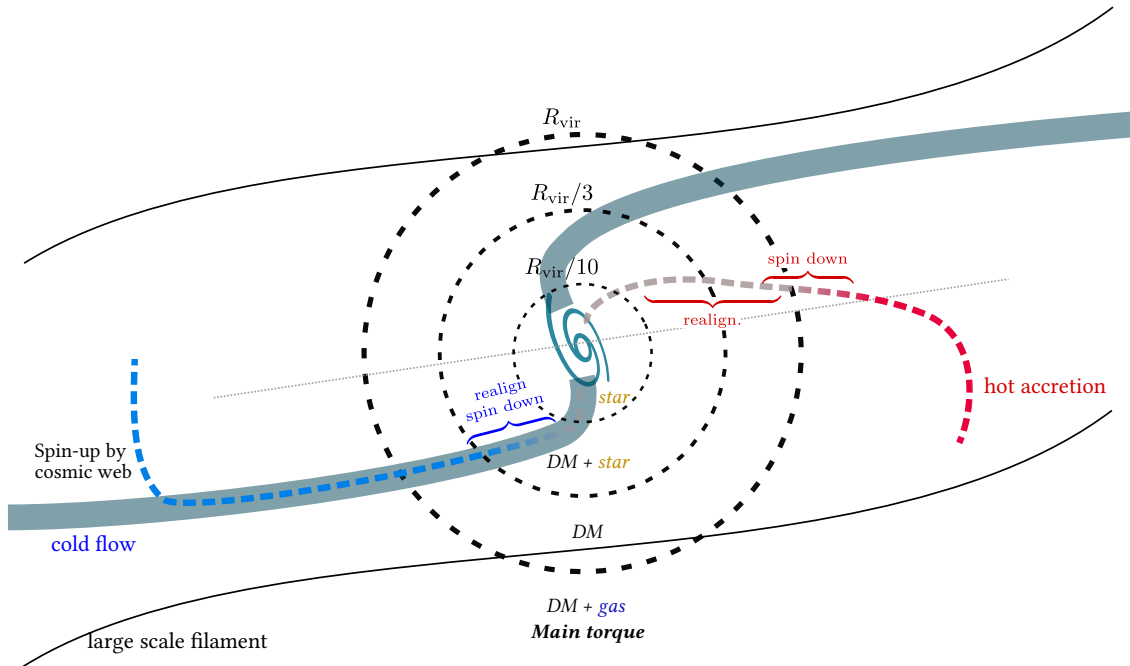


Figure 6.5.1: Sketch of the evolution of the AM at large z (not to scale). hot gas (red dashed line) is spun-up by the cosmic web and loses most of its AM at the virial radius in the shock. Cold gas (blue dashed line) is spun-up by the cosmic web and retains its AM down to the inner halo. Between the inner halo and the disk, most of the AM is lost due to interactions with the DM halo and the disk.

Using a set of high-resolution zoom-in simulations, I have studied the evolution of the AM of gas accreted via the cold and the hot mode around six group progenitors at $z \gtrsim 2$. I also presented new numerical methods to extract the contributions of the different forces and torques (gravitational and pressure torques). My findings are the following:

1. the magnitude of the sAM of the cold gas is conserved down to the inner halo, the magnitude of the sAM of the hot gas is lost outside the halo,
2. the orientation of the sAM of the cold gas is conserved down to the inner halo,
3. the sAM of the hot gas is significantly less aligned to the large scale environment,
4. the dominant local forces in the cold gas are pressure forces and DM gravitational forces in the outer halo, and DM gravitational and stellar gravitational forces in the inner halo and the disk,
5. though, the pressure forces lack a spatial structure, so that their net contribute averages out in the cold gas,
6. therefore, the dominant torques in the cold cold gas are gravitational torques: DM gravitational torques dominate in the outer halo, stellar gravitational torques dominate in the disk.

The results on the major torques are sketched on figure 6.5.1. My findings indicate that the acquisition of the AM for group progenitors at $z \gtrsim 2$ is driven by the AM acquired at large-scale, consistent with the findings that the spin of galaxies is aligned with their environment. Most of the AM is able to flow down to the inner halo where gravitational torques redistribute it to the DM and the disk component, effectively transporting AM from the scales of the cosmic web to the scales involved in disk formation. These findings indicate that galaxy formation models aimed at

understanding AM acquisition should take into account the cold accretion mode, at least at high redshift. I have underlined that AM acquisition is dominated at large scales by the interaction with the cosmic web. In the halo, the evolution of the sAM of the cold flows is dominated by interactions with the inner halo and the disk. The sAM of the hot-accreted material is dominated by its interaction with the halo.

This work is part of an on-going research effort. In particular, a significant part of my work has been devoted to the development of new numerical methods to enable researchers and myself to study the complex problem of the accretion of angular momentum. In particular, I have illustrated that its evolution is driven by subtle complex interactions, which can now be captured and studied in details, in particular using AMR codes.

6.A Additional material

In this section, I provide additional material. Figures 6.A.1a and 6.A.1b present mass-weighted projections of the magnitude of the pressure gradients and of the DM gravitational forces for halo A. They complement figure 6.3.1 by providing views in the xz and yz planes. In particular, the structure of the pressure ring is clearly visible in the pressure plots and not visible at all in the gravitational forces plots. Figures 6.A.2a and 6.A.2b present the evolution of the torques projected on the AM vector of the galaxy at $z = 2$ for halos A and B. The evolution of the torques projected on the axis of the galaxy are qualitatively similar for halos A and B.

A visualization of the cosmic web, showing a complex network of glowing yellow and orange filaments and nodes against a dark background with faint galaxies.

7. Conclusion

Yohan Dubois – New Horizon collaboration

7.1 Closing remarks

The value of science lays in its predictive power. Hence, in the context of structure formation, a central question that theoretical cosmology must address is the following: to what extent can today's properties of galaxies be predicted from the initial Gaussian random field from which they emerge? More specifically, how can one encode the initial conditions in a compressed way to predict the fate of galaxies that will emerge from them? One of the success of the Λ CDM model is its ability to predict a significant number of properties of DM halos and their galaxies. In the classical model of galaxy formation, galaxy form out of the condensation of the gas in the potential well of their host halo. As such, galaxy properties are usually understood as a result of the halo mass – which sets the amount of gas available and the internal kinematics – and the local density – which regulates gas accretion and pair interactions. The classical analytical and semi-analytical models intrinsically suppose that halo properties, and as a consequence, galaxy properties are only influenced by their local environment via the local density, with some extensions probing also the local tidal environment. These models has proven successful at predicting a large number of galactic properties, such as their spatial clustering or their mass function. The detailed modelling of the evolution of the baryons on galactic scales is key to the success of these models, yet more work needs to be done to include the effects underlined in this dissertation.

However, it has been established that the clustering of dark matter halos, as measured by halo bias, not only depends on halo mass but also on other halo properties such as formation time, concentration, spin and ellipticity (Gao et al., 2005; Wechsler et al., 2006; Gao and S. D. M. White, 2007; Hahn et al., 2007). This problem, commonly referred to as the “assembly-bias problem” can be rephrased as follow: the clustering of dark matter halos and their properties are correlated, beyond a mere mass and density relation. On large scales, systematic galactic surveys (de Lapparent et al., 1986; Geller and Huchra, 1989; Colless et al., 2001; Tegmark et al., 2004; Abazajian et al., 2003) have revealed that the Universe is structured around voids, sheets, filaments and knots that form the cosmic web. Using a different approach, a growing number of evidence have since showed that some halo and galaxy properties present distinct features at different locations in the cosmic web. As presented in Kraljic et al., 2018, void galaxies are found to be less massive,

bluer and more compact than galaxies outside of voids (Rojas et al., 2004; Beygu et al., 2016); galaxies infalling into clusters along filaments show signs of some physical mechanisms operating even before becoming part of these systems, that galaxies in the isotropic infalling regions do not (Porter et al., 2008; Martínez et al., 2016); Kleiner et al., 2017 find systematically higher HI fractions for massive galaxies near filaments compared to field population, interpreted as evidence for a more efficient cold gas accretion from the intergalactic medium. A small but significant trend in the distribution of galaxy properties within filaments was reported in the spectroscopic surveys VIPERS (Malavasi et al., 2017) and GAMA (Kraljic et al., 2018) and with photometric redshifts in the COSMOS field (Laigle et al., 2018). These studies find significant mass and type segregations, where the most massive or quiescent galaxies are closer to filaments than less massive or active galaxies, emphasizing that large-scale cosmic flows play a role in shaping galaxy properties. On the other hand, other works reported that the most important driver of galaxy properties is stellar mass, as opposed to environment (Robotham et al., 2013; Alpaslan et al., 2015; Alpaslan et al., 2016), while the environment may impact the efficiency of galaxy formation (Guo et al., 2015; Eardley et al., 2015).

On large scales, the TTT naturally connects the distribution of matter to the angular momentum of halos (see section 2.1.6) in its recently revisited, conditioned formulation (Codis et al., 2015), with low-mass galaxies being preferentially aligned with filament's direction while more massive ones have their spin perpendicular to it. While it is far from obvious that the alignment of halo spin implies that the galactic spin are also aligned, the effect has also been confirmed for galaxies in numerical simulations (Dubois et al., 2014; Welker et al., 2014a) and recently observationally (e.g. Trujillo et al., 2006; Lee and Erdogdu, 2007; Paz et al., 2008; Tempel et al., 2013; Tempel and Libeskind, 2013; Pahwa et al., 2016, see also for B. J. T. Jones et al., 2010; Cervantes-Sodi et al., 2010; Andrae and Jahnke, 2011; Goh et al., 2019 contradictory results).

In the context of assembly bias, many extensions of the halo model have been suggested to understand the modulation effects of the cosmic web in terms of local properties. In particular, it has suggested that the local tidal field may explain part of the assembly bias signal (e.g. Hahn et al., 2009; Ludlow et al., 2014) when formulated in terms of the formation time. Tidal forces induce a shear flow in the vicinity of small halos that flow along filaments of the cosmic web. One of the outcomes is that the accretion rate of small halos is decreased by neighbouring structures, so that small halos growing in dense environments are not able to accrete mass. As a consequence, these halos appear older resulting in a differential biasing as a function of formation time. In a similar way, Paranjape et al., 2018 suggested that the effect of halo concentration on the bias is well explained by a local quantification of the local tidal anisotropy. All these models are typically extensions of the halo model with new halo-centred probes of the larger-scale environment.

Another possible approach followed in this dissertation is to relax the halo-centric assumption and work in the frame that sets the large scale environment: the cosmic web. Indeed, due to the statistical properties of the initial conditions of the Universe, the different scales involved in galaxy formation and the formation of the cosmic web are coupled statistically. In particular, large-scale structures such as large filaments have an impact on the statistical properties of the field out of which halos grow, which has the effect of biasing halo assembly. One can argue that the assembly signal can be explained simply *via* this biasing effect of the cosmic web: the cosmic web is responsible for driving the typical assembly history at fixed halo mass and local density.

This approach has already proven successful at providing a theoretical explanation to the spin-alignment problem (Codis et al., 2015). In this dissertation, I argued that the problem stated in these terms can also provide a valuable understanding of how halos grow, but also how their galaxy forms. Using an extension of the excursion set theory (Bond et al., 1991; Lacey and Cole, 1993; Mo and S. D. M. White, 1996), I showed in chapter 4 (Musso, Cadiou et al., 2018) that the

cosmic web, and in particular large scale filaments, biases the formation of dark matter halos. The formalism predicts that the variables entering the assembly history of the halo, namely the halo formation time and the accretion rate, are modulated by the cosmic web. As a result, at fixed final mass, halos forming close to nodes of the cosmic web are found to accrete more and have formed at later times, in agreement with N -body simulations for large-mass halos (R. K. Sheth and Tormen, 2004; Gao et al., 2005; Wechsler et al., 2006; Dalal et al., 2008). This effect complements other suggestions that the tide may be responsible for the assembly bias signal as it is purely geometric: as halos grow by accreting material, they also probe larger scales whose statistical structure is set by the cosmic web. I also argued that this provides a natural frame in which the assembly signal is simply a spatial modulation, or stated differently, different assembly histories are to be expected at different locations. This framework has since been used to show that, in hydrodynamical simulations, the cosmic web has also an effect on the assembly of galaxies. In Kraljic et al., 2019, appendix B.2, we reported that the specific star formation rate and the velocity-to-velocity-dispersion ratio both present significant modulations in along the filaments, highlighting that, indeed, filamentary structures can be used as a metric to parametrize the assembly of dark matter halos and galaxies therein.

Although a number of evidences are pointing towards an effect of the cosmic web on galaxy formation, the detailed physics that couples them is still poorly understood. One of the issues lays in the description of the cosmic web itself, so that different methods may lead to different effects on galaxy formation. One key parameter to further study the effect of the cosmic web is then the question of its description, the challenge residing in its continuous and multi-scale nature. A large number of methods have been developed to tackle this issue and provide a local frame in which galaxy properties can be studied (Bond et al., 1996; Sousbie et al., 2008 and Libeskind et al., 2018 for a review). In my dissertation, I suggested a new relevant parameter entering the formation of galaxies and dark halos, namely the evolution of the cosmic web. I presented compact theoretical predictions to account for it in a compact way and provide theoretical predictions of the evolution of the cosmic web in the Lagrangian space of the initial conditions (based on the idea of Hanami, 2001) and linked them to the connectivity of the cosmic web (Codis et al., 2018). Using an extension of the theory to the mildly non-linear regime, I showed that one can connect our predictions to results obtained from N -body simulations. In particular, the formalism is able to detect halo merger events, but also filament- and wall-mergers in the Lagrangian initial conditions. I argued that these events, named “critical events”, whose theory was developed in chapter 4, may be relevant parameters entering galaxy models, in particular to understand the evolution of galaxy properties that depend on the geometry of the accretion (such as their spin or their velocity-to-velocity-dispersion). This could readily be used to constrain further the assembly of dark matter halo by providing variables describing the evolution of the environment.

In the current understanding of galaxy formation, the evolution of the baryons is driven by the cosmic web on large scales, while at small scales complex interactions between the gas, stars and AGNs and the dark matter halo drive most of the physics. While the impact of the cosmic web on halo formation can be studied to some extent from first principles as I have demonstrated in chapters 3 and 4, the complex baryonic physics at play make the task much more complex on smaller scales. This problem is usually tackled using hydrodynamical cosmological simulations that reproduce as accurately as possible galaxy formation in a realistic cosmological context. In this approach, a single testbed can be used to probe at the same time halo formation and galaxy formation. One of the questions these simulations can answer is linking dark matter halos and their galaxies. One particular example, relevant to the formation of disks, is the spin of galaxy, which is found to be only weakly correlated to the halo disk (Hahn et al., 2010; Jiang et al., 2018). The inner halo’s spin is well correlated with the galactic spin, which, at large redshifts is also well correlated to the principal axis of the large-scale tidal field. It has been suggested that one

way for galaxies to grow a disk independently from their host halo's spin is through cold flows, which are the main driveway to funnel angular-momentum rich material from the cosmic web down to the innermost regions of the galaxies (Tillson et al., 2015; Nelson et al., 2015; Danovich et al., 2015), effectively connecting the large-scale environment to the spin of galaxies. Indeed, if the accretion history of the cold gas differs from that of the hot gas and DM, it can be expected that the response of the galaxy to the large scale perturbations will also be different, resulting in a differential evolution of the halo and its galaxy. Using a suite of numerical simulations and novel numerical methods to trace the Lagrangian trajectories of gas elements in an adaptive mesh refinement code (chapter 5, Cadiou et al., 2019), I have studied the formation of disk galaxies at large redshift and showed that the information acquired by the gas at large scale is transported to the inner regions of the halo and in the galaxy (chapter 6). In particular, cold flows are able to retain most of their angular momentum down to the inner halo. In the inner halo and around the disk, complex gravitational torques redistribute the angular momentum to the inner halo and the stellar component. I argue that this may lead to a good alignment of the inner halo and the galaxy, since their angular momentum is partially driven by their interaction with cold flows. This internal alignment is also expected to reflect the large-scale tidal field set by the cosmic web, as most of the anisotropic information is transported to the internal regions.

As a final conclusion, I have shown that the cosmic web is able to influence the assembly of dark matter halos. One can build theoretical models in which part of the assembly bias can simply be interpreted as a large-scale environment modulation, which cannot be parametrized easily in terms of the local properties of the field, both for dark matter halos and galaxies. I proposed a set of parameters that are suited to the compact description of the evolution of the cosmic web and I argue that the geometry of the accretion onto galaxies via cold flows, and its evolution, can have a significant impact on the properties of galaxies, in particular against the ones sensitive to the anisotropy of the flows. This is in particular highlighted by a numerical study that showed that the angular momentum of the gas, set by the cosmic web, is effectively transported down to the galaxy where complex interactions redistribute it. I suggest that in order to capture effects beyond mass and density relations, models of galaxy and halo formation should be augmented by parameters describing the non-local structure of the cosmic web at large-scales in terms of its critical points (nodes, filament and wall centers) but also in terms of their evolution, as described by critical events.

7.2 Perspectives and applications of my work

Let me present possible applications and further developments of the results presented in this thesis. Indeed, a significant part of my work was devoted to the building different tools (constrained excursion set theory, critical event theory, Monte Carlo tracer particles) that have already been embraced by other researchers in the field: this should enable us to soon produce new results in the context of galaxy formation and large scale structure hydro dynamics. Let me briefly detail a couple of such possible extensions.

7.2.1 Extensions of the constrained excursion set theory

On the theoretical side, the predictions on assembly bias have proven quite successful at providing a physical understanding of the effect of the cosmic web on halo formation (Kraljic et al., 2018; Kraljic et al., 2019, see appendices B.1 and B.2). There is however room for further improvement to get a more refined model. One possible extension would require to take into account ellipsoidal collapse (Hahn and Paranjape, 2014; Ludlow et al., 2014; Ramakrishnan et al., 2019). As a first step, one could extend the work of chapter 4 with a barrier that depends on the *mean* tidal structure of the field. While this would not provide a definitive answer, one would recover the predictions

of Musso et al., 2018 with an extra modulation coming from the mean tidal environment in the form of a shifted, spatially-modulated barrier $\delta_c \rightarrow \delta_c(\mathbf{r})$, where \mathbf{r} is the distance to the nearest structure. This would likely have the consequence of delaying collapse in high-tide regions. Another possible approach to the problem of the tides on the collapse of halos is to rely on a Monte-Carlo sampling to explore the different excursion trajectories constrained to their large-scale environment. One could then seek the first-crossing given a barrier that is itself a random variable of the smoothing scale. In addition to explicitly taking into account ellipsoidal collapse and the effect of tides, this would also enable us to use the first-crossing condition instead of an approximation, so that the results could be extended to smaller masses. A detailed study would also require to take into account the Zel'dovich displacement, and in particular study the effect of a galaxy travelling from voids to sheets to filaments to nodes, as significant relative velocities can be obtained by the travelling galaxy (in the spirit of the peak patch theory, Bond and Myers, 1996) which may explain the presence of quenched halos at the geometrical center of filaments (Borzyszkowski et al., 2017; Romano-Díaz et al., 2017; Garaldi et al., 2018).

7.2.2 Following dust formation using Monte-Carlo sampling methods

The Monte Carlo tracer particle, described in chapter 5, have obviously a broad range of applications. They have already been used to follow the formation and disruption of clumps in Coma-like clusters (Beckmann et al., submitted, appendix B.3). The problem of following the Lagrangian history of elements in a Eulerian framework should also find applications in coupled dust grain-gas models. In particular, bi-fluid models of strongly coupled dust and gas mixtures are difficult to integrate numerically. For Lagrangian-based methods they tend to produce spurious dust aggregates when the grains are accumulated below the resolution length of the gas (Ayliffe et al., 2012). In AMR codes, it was recently proposed to treat the dust-gas mixture as a single fluid with a diffusion term fluid instead (Lebreuilly et al., 2019), yielding accurate results for strongly coupled (small) grains. This method however requires one fluid per grain size bin, so that the treatment of a large range of grain size quickly becomes tedious. In order to circumvent this problem, one could modify the Monte Carlo approach of chapter 5 to follow individual dust grains with arbitrary grain size distribution. One would have to modify the transition probability involved in the tracer particle scheme (equation 5.1) to account for the relative drift of the dust grain with respect to the gas.

7.2.3 Critical events as input to Machine learning and Bayesian inference

The physics of galaxies is largely driven by non-linear processes (gas cooling, feedback, star formation). In order to capture these processes, we usually make use of numerical simulations that reproduce the known physics and can later be used to learn which processes are key to galaxy formation. In particular, I argue that some properties of galaxies, and in particular vector quantities (the spin) or those sensible to the recent accretion history (v/σ , star formation rate) can be better understood if one takes into account the merger history of the halo *and* its environment. Indeed, there is a long tradition of relying on merger trees of dark halos extracted from simulations as a mean to predict the physical properties of galaxies (with so-called semi-analytical models, see e.g. Benson, 2010, and reference therein). One of the long term main motivations for the present work is to extend this strategy to the other two merger trees (filaments and walls), and to rely on modern segmentation techniques to identify which combination of events are most likely to lead to galaxies of a certain type to be produced in cosmological simulations. This strategy is likely to be efficient and rewarding, as the set of critical events is a very strong compression of the initial conditions, and because once the segmentation has been done, the subset of events which are in the past lightcone of a galaxy with a given tag have physical meaning. For instance, recent disconnection of filaments at a given smoothing scale are likely to impact gas infall at

the redshift of corresponding smoothing scale, hence associated galaxy star formation and disc reformation. The set of critical events represents a useful effective topological compression of the initial conditions which will impact the upcoming ‘dressed’ mergers (*i.e.* the cosmic evolution of peaks *and* their filaments and walls). Note that the exact relative configuration of critical events in the smoothing-position space may be of relevance, and is not fully captured by the sole knowledge of the one and two-point statistics. Since the link between the galaxy formation and their properties is still poorly understood, a model agnostic approach can be used to study the effect of critical events on galaxy formation.

Predicting galactic properties using machine learning

In order to assess this, we can rely on machine learning techniques. Let me illustrate the strategy one could use using a catalogue of synthetic galaxies from a cosmological simulation. Let me assume that a set of virtual galaxies have been classified with a continuous parameter, e.g. based on their morphology via their kinematic properties, v/σ . This ratio is computed from the 3D velocity distribution of stellar particles of each galaxy. In the frame of the angular momentum of that galaxy, the velocity is decomposed into cylindrical components v_r, v_θ, v_z , and the rotational velocity of a galaxy v is defined as the mean of v_θ of individual stars. The average velocity dispersion of the galaxy $\sigma^2 = (\sigma_r^2 + \sigma_\theta^2 + \sigma_z^2)/3$ is computed using the velocity dispersion of each velocity component σ_r, σ_θ and σ_z . This ratio allows me to separate rotation-dominated ($v/\sigma \gg 1$) from dispersion-dominated ($v/\sigma \ll 1$) galaxies. For each central galaxy identified in the simulation, one can identify their corresponding dark matter halo to trace the Lagrangian patch of dark matter particles back into the ICs. This defines a connected gravitational patch that contains all critical events in causally connected to the final galaxy. Hence, the simulation provides me with a set of relations for k patches and three types of critical events $j \in [\mathcal{P}, \mathcal{F}, \mathcal{W}]$

$$\left(\{ \Delta \mathbf{r}_{j,i}, R_{j,i}, \nu_{j,i} \}_{i \leq n_{j,k}} \right)_{j \in [\mathcal{P}, \mathcal{F}, \mathcal{W}]} \rightarrow (v/\sigma)_k, \quad (7.1)$$

where $\Delta \mathbf{r}_{j,i}$ is the relative position *within the patch* of the critical event i of type j measured w.r.t. the centre of mass of the patch, $\nu_{j,i}$ is its contrast, and $R_{j,i}$ the corresponding smoothing scale, while v/σ_k is the velocity ratio of the patch k . Let me call \mathcal{E}_k the l.h.s. of this relation. Standard machine learning tools (random tree forest, stochastic gradient descent), allows me to build a predictor, $P_r(\mathcal{E})$ from a subset of $(\mathcal{E}_k \rightarrow v/\sigma_k)_{k \leq K_{\text{train}}}$ drawn randomly from the full sample. From this training, one can do one of two things: i) use it as a predictor to associate $(v/\sigma)_k$ to other patches for which we computed their set of events, \mathcal{E}_k . ii) identify which features in this event set is responsible for the corresponding value of v/σ .

The former approach would be useful to find regions of interest in the initial conditions, therefore avoiding a costly try-and-error approach. For example, this could provide a likelihood of finding a galaxy with given morphology in the initial conditions, so that only regions of interest are resolved with high resolution. This is usually tackled by running larger than necessary simulations, in which only the regions of interest are kept *a posteriori*. While the approach suggested here would still have a chance of failing, it could significantly decrease the computation volume required to simulate a given configuration and could complement other approaches, such as genetically modified initial conditions (Roth et al., 2016; Rey and Pontzen, 2017). This could also provide useful insight to understand which halos host early SMBHs. Indeed, it was recently proposed (Huang et al., 2019) that the structure of the initial conditions precondition the early evolution of SMBHs in numerical simulations, while another study showed that the environment has an impact on AGN properties (Porqueres et al., 2018; Man et al., 2019). This problem is tightly coupled to the problem of feeding galaxies with fresh gas, which, at high-redshift, is linked to the orientation and structure of the local cosmic web via cold filamentary accretion. Here I argue that critical events are useful tools to study this class of problem, in particular at high redshifts.

The latter approach could be implemented over sets of simulations which implement different feedback recipes as a mean of disentangling the relative impact of environment and sub-grid physics on the evolution of galaxies

Critical events as input to Bayesian framework

Let me illustrate how one could use critical events to study the susceptibility of a set of galactic parameters to their cosmic web environment. Using a similar approach as described in the previous paragraph, the sample can be used decomposed as a set of inputs and output variables \mathbf{X} , \mathbf{Y} , treated here as random variables

$$\mathbf{X}_j^{(0)} = \{M_j, \rho_j\}, \quad \mathbf{X}_j^{(1)} = \{\{\Delta \mathbf{r}_{i,j}, R_{i,j}, \nu_{i,j}, k_{i,j}\}_{i=1, \dots, N_j}\}_j, \quad \mathbf{Y}_j = (v/\sigma)_j. \quad (7.2)$$

where $\Delta \mathbf{r}_{j,i}$ is the relative position *within the patch*, $R_{i,j}$ is the smoothing scale, $\nu_{i,j}$ is the density contrast and $k_{i,j}$ is the kind ($k \in [\mathcal{P}, \mathcal{F}, \mathcal{W}]$) of the critical event i . Here I have split the inputs between the variables commonly included in galaxy formation models, the mass of the halo M_j and the density ρ_j , which I named $\mathbf{X}_j^{(0)}$. The input variable $\mathbf{X}_j^{(1)}$ contains the ‘‘augmented’’ past history as encoded by the N_j critical events found in the Lagrangian patch of galaxy j . The output variable is chosen here to be v/σ , but it could be any other galactic property, such as the bulge mass or the SMBH mass. Using the concept of cross-entropy, one can then compute the information gain on the distribution of v/σ when adding to the classical mapping $\mathbf{X}^{(0)} \mapsto \mathbf{Y}$ the augmented merger tree $(\mathbf{X}^{(0)}, \mathbf{X}^{(1)}) \mapsto \mathbf{Y}$. The cross-entropy will tell us how many more bit of (Shannon) information is gained by adding the information from the merger history of the cosmic web in the gravitational patch of the galaxy. This can then be further extended by segmenting $\mathbf{X}^{(1)}$ into subsets containing only halo mergers, filament mergers and wall mergers to quantify which event better encodes the parameter v/σ .

Beyond the scope of this work, when co-analysing the evolution of galactic properties with critical point mergers, one could relate the various (filament, wall) mergers to special events in terms of change in connectivity and feedback (e.g. the destruction of filaments by AGN activity, see Dubois et al., 2013). It could also be interesting to see if spin flip correlates with filaments or wall vanishing.